



Title	Pavement design method in Japan with consideration of climate effect and principal stress axis rotation
Author(s)	Lin, Tianshu; Ishikawa, Tatsuya; Maruyama, Kimio; Tokoro, Tetsuya
Citation	Transportation geotechnics, 28, 100552 <a href="https://doi.org/10.1016/j.trgeo.2021.100552">https://doi.org/10.1016/j.trgeo.2021.100552</a>
Issue Date	2021-05
Doc URL	<a href="http://hdl.handle.net/2115/88577">http://hdl.handle.net/2115/88577</a>
Rights	© <2021>. This manuscript version is made available under the CC-BY-NC-ND 4.0 license <a href="http://creativecommons.org/licenses/by-nc-nd/4.0/">http://creativecommons.org/licenses/by-nc-nd/4.0/</a>
Rights(URL)	<a href="http://creativecommons.org/licenses/by-nc-nd/4.0/">http://creativecommons.org/licenses/by-nc-nd/4.0/</a>
Type	article (author version)
File Information	Manuscript-Lin Tianshu-revised.pdf



[Instructions for use](#)

1 Pavement design method in Japan with consideration of climate effect and principal stress axis  
2 rotation

3

4 Tianshu Lin <sup>a</sup>, Tatsuya Ishikawa <sup>b\*</sup>, Kimio Maruyama <sup>c</sup>, Tetsuya Tokoro <sup>d</sup>

5 <sup>a</sup> Graduate School of Engineering, Hokkaido University, Kita 13, Nishi 8, Kita-Ku, Sapporo  
6 060-8628, Japan

7 <sup>b</sup> Faculty of Engineering, Hokkaido University, Kita 13, Nishi 8, Kita-Ku, Sapporo 060-8628,  
8 Japan

9 <sup>c</sup> Cold-Region Maintenance Engineering Research Group, Civil Engineering Research Institute  
10 for Cold Region, 1-34, Hiragishi 1, 3, Toyohira-ku, Sapporo 062-8602, Japan

11 <sup>d</sup> Faculty of Engineering, Hokkai-Gakuen University, 1-1, Minami 26 Nishi 11, Chuo-ku, Sap-  
12 poro 064-0926, Japan

13 **Key words**

14 Rutting; Fatigue cracking; Freeze-thaw action; Resilient modulus; Mechanical-empirical de-  
15 sign method

16 **Abstract**

17 Current Japanese design guide uses mechanical-empirical criteria to predict the failure loading  
18 number against fatigue cracking and rutting. However, these criteria have some limitations that

---

\* Corresponding author. Email address: t-ishika@eng.hokudai.ac.jp

19 the variation in moduli of base and subgrade layer due to the fluctuation in water contents,  
20 freeze-thaw history, and stress states are not considered. As well known, these factors greatly  
21 affect the soil mechanical properties like resilient modulus. Besides, present rutting failure cri-  
22 terion provides no indication of the behavior of rutting over time, and the effect of principal stress  
23 axis rotation on rutting development is also not captured. To overcome such limitations, this study  
24 modified the present Japanese pavement design method through the following two main aspects:  
25 (1) Replacing constant elastic modulus of base and subgrade layer to resilient modulus related  
26 to stress states and complex climate conditions, which are defined as the combination of fluc-  
27 tuating water content and freeze-thaw action; (2) Modifying rutting failure criterion by consid-  
28 ering generally used MEPDG model and also the effect of principal stress axis rotation. All  
29 modifications are performed based on laboratory element test like suction-controlled freeze-  
30 thaw triaxial test, which could simulate complex climate conditions, and multi-ring shear test,  
31 which could simulate principal stress axis rotation. Besides, modified criteria are examined by  
32 comparing to long-term measured performance of test pavements built in Hokkaido, the north  
33 island of Japan. Modified Japanese pavement design method shows high applicability and ac-  
34 curacy on the pavement life prediction, especially for the flexible pavement in cold regions like  
35 Hokkaido.

## 36 **1. Introduction**

37 Mechanistic-Empirical Pavement Design Guide (MEPDG), which combines empirical and  
38 mechanistic concepts, uses input data such as materials, traffic, climate, and for a trial design  
39 calculates mechanistically stresses and strains, which are subsequently used in empirical

40 distress models to compute damage accumulated over time like rutting, fatigue cracking, and  
41 thermal cracking. MEPDG has been mainly used in the United States. At the current time with  
42 regard to Japan, a mechanistic-empirical method based only on a multi-layer linear elastic  
43 model is still currently being used and as a consequence, the applicability and prediction preci-  
44 sion are unsatisfactory.

45 To be precise, several serious drawbacks limit the applicability and accuracy of present Japa-  
46 nese pavement design method. First, constant base and subgrade layer moduli through the  
47 whole year based on linear elastic theory restrict the precision since soil shows nonlinear elastic  
48 property in small strain period as reviewed by Clayton [2011]. Based on such nonlinearity,  
49 resilient modulus ( $M_r$ ) is proposed [Seed, 1955] to capture the effect of stress states on the  
50 stiffness of soil.  $M_r$  is widely used in Mechanistic-Empirical Pavement Design Guide (MEPDG)  
51 and estimated by Eq. (1), named as the universal model [AASHTO, 2008]. According to Eq.  
52 (1), the resilient modulus decreases with increasing deviator stress and decreasing confining  
53 pressure. In general, based on laboratory element test results, resilient modulus of base course  
54 and subgrade material are determined and employed as the layer moduli in a multi-layered  
55 elastic pavement response model.

$$56 \quad M_r = k_1 p_a \left( \frac{\theta}{p_a} \right)^{k_2} \left( \frac{\tau_{oct}}{p_a} + 1 \right)^{k_3} \quad (1)$$

57 where  $k_1$ ,  $k_2$ ,  $k_3$  are regression constants;  $p_a$  is atmospheric pressure and set as 101 kPa in this  
58 study;  $\theta$  is bulk stress (kPa);  $\tau_{oct}$  is octahedral stress (kPa).

59 Second, effects of water content and freeze-thaw action, which greatly influence the stiffness of  
60 base and subgrade layer [Berg et al., 1996; Cole et al., 1981; Johnson et al., 1978; Simonsen et  
61 al., 2002; Simonsen and Isacsson, 2001], are not considered in Japanese pavement design method.

62 To be precise, rising water content, as a result of the inflow of water during rainfall or the  
63 thawing of ice lenses, causes a temporary decrease in the stiffness of base course and subgrade  
64 materials. Meanwhile, freeze-thaw action always decreases moduli of base and subbase layer  
65 materials even with no excess water storage after thawing [Ishikawa et al., 2019a; Lin et al.,  
66 2019b], as ice formation tends to break some of the particle contacts and interlocking of soil  
67 particles and finally deteriorates the soil structure uniformity and stiffness.

68 Third, current rutting model cannot capture the behavior of rutting over time or with the applica-  
69 tion of traffic loading. It also does not consider rate-hardening or the contribution of the non-  
70 subgrade layers to rutting. To overcome these limitations, MEPDG proposed a rutting depth pre-  
71 diction model [NCHRP, 2004], which converts the plastic strain measured from the laboratory  
72 to the field condition, as shown in Eq. (2).

$$73 \quad \varepsilon_p(N) = \beta_1 k_1 \left(\frac{\varepsilon_0}{\varepsilon_r}\right) e^{-\left(\frac{\rho}{N}\right)^\beta} \varepsilon_v \quad (2)$$

74 where  $\varepsilon_p(N)$  is permanent strain for the layer/sub-layer;  $N$  is number of traffic repetitions;  $\varepsilon_0$ ,  $\beta$ ,  
75 and  $\rho$  are material properties;  $\varepsilon_r$  is resilient strain imposed in laboratory test to obtain material  
76 properties  $\varepsilon_0$ ,  $\beta$ , and  $\rho$ ;  $\varepsilon_v$  is average vertical resilient strain in the layer, which is calculated by  
77 a multi-layer elastic pavement response model;  $\beta_1$  is calibration factor for the unbound granular  
78 and subgrade materials;  $k_1$  is global calibration coefficients.

79 Last, the rutting failure criterion in Japanese pavement design guide as well as MEPDG rutting  
80 model does not capture the effect of principal stress axis rotation (PSAR), which is a phenom-  
81 enon caused by moving wheel loads and greatly amplifies the permanent deformation of base  
82 and subgrade layer [Miura et al., 1986; Brown, 1996; Gräbe and Clayton, 2009; Inam et al.,  
83 2012; Ishikawa et al., 2011, 2019b; Lin et al., 2019a]. This is because the conventional rutting

84 models are mainly built on traditional repeated loading triaxial test with constant confining  
85 pressure and no principal stress axis rotation.

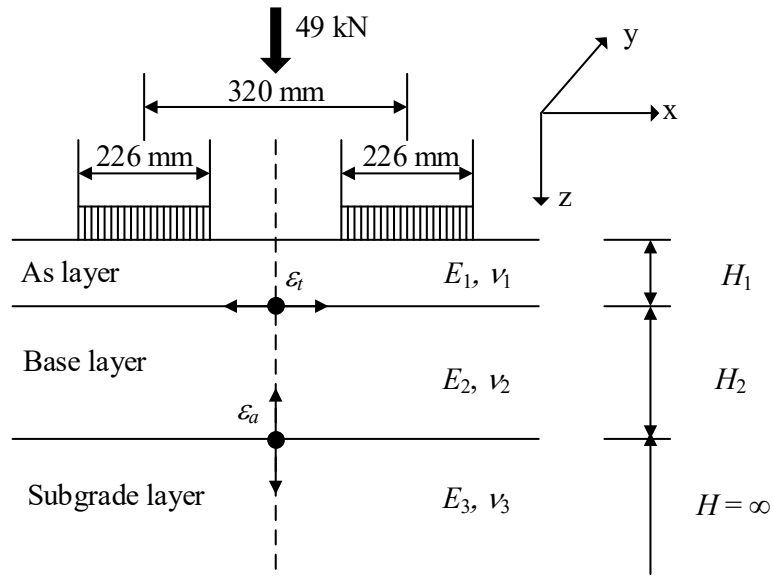
86 Consequently, to overcome aforementioned limitations, this study modified the present Japa-  
87 nese pavement design method through two main aspects: (1) Replacing constant elastic modu-  
88 lus of base and subgrade layer to resilient modulus related to stress states and complex climate  
89 conditions, which are defined as the combination of fluctuating water content and freeze-thaw  
90 action. To be precise, Ishikawa et al. [2019a] and Lin et al. [2020] studied the synergistic effect  
91 between water content and freeze-thaw action, named as climate effect, on the base course and  
92 subgrade materials. This study combined these research results to determine the base and sub-  
93 grade layer moduli with complex water content and freeze-thaw conditions. (2) Modifying rut-  
94 ting failure criterion by considering generally used MEPDG model and also the effect of prin-  
95 cipal stress axis rotation. To be precise, this study modified the structure of present rutting  
96 model referring to MEPDG rutting model. Furthermore, the amplification of permanent defor-  
97 mation caused by PSAR is examined through laboratory test results. Such effect caused by  
98 PSAR was also used to modify the structure of rutting failure criterion in this study. This study  
99 specially focuses on the pavement life against rutting since modification of the fatigue cracking  
100 model is done by previous researches [Maruyama et al., 2006, 2008].

## 101 **2. Applicability of present Japanese pavement design method**

### 102 2.1 Present Japanese pavement design method

103 Japanese pavement design method [JRA, 2006] provides rutting and fatigue cracking failure  
104 criteria, as shown in Eqs. (3) to (5) and (6) to (13), to calculate allowable loading number of

105 equivalent 49-kN wheel loads against rutting ( $N_{fs}$ ) and fatigue cracking ( $N_{fa}$ ). These allowable  
 106 loading numbers are calculated by a theoretical design method, also known as AI model, [As-  
 107 phalt Institute, 1982] using a simplified three-layers model which consists of asphalt mixture  
 108 layer (hereafter referred to as the “As layer”), base layer, and subgrade layer as shown in Fig.  
 109 1.



110

111 Fig. 1 Three-layers model for allowable loading number calculation.

112 
$$N_{fs} = \beta_{s1} \cdot \{1.365 \times 10^{-9} \cdot \varepsilon_a^{-4.477 \cdot \beta_{s2}}\} \quad (3)$$

113 
$$\beta_{s1} = 2134 \quad (4)$$

114 
$$\beta_{s2} = 0.819 \quad (5)$$

115 
$$N_{fa} = \beta_{a1} \cdot C \cdot \{6.167 \times 10^{-5} \cdot \varepsilon_t^{-3.291 \cdot \beta_{a2}} \cdot E_1^{-0.854 \cdot \beta_{a3}}\} \quad (6)$$

116 
$$C = 10^M \quad (7)$$

117 
$$M = 4.84 * \left( \frac{VFA}{100} - 0.69 \right) \quad (8)$$

118 
$$\beta_{a1} = K_a * \beta_{a1}' \quad (9)$$

$$119 \quad K_a = \begin{cases} \frac{1}{8.27 \times 10^{-11} + 7.83 \cdot e^{-0.11 H_a}}, & H_1 < 0 \\ 1, & H_1 \geq 0 \end{cases} \quad (10)$$

$$120 \quad \beta_{a1}' = 5.229 \times 10^4 \quad (11)$$

$$121 \quad \beta_{a2} = 1.314 \quad (12)$$

$$122 \quad \beta_{a3} = 3.018 \quad (13)$$

123 where  $\beta_{s1}$ ,  $\beta_{s2}$ ,  $\beta_{a1}$ ,  $\beta_{a2}$ , and  $\beta_{a3}$  are the compensation rates for AI failure criteria based on the  
 124 actual situation of Japanese pavement;  $C$  is the material parameter;  $M$  is a factor relates the  $VFA$   
 125 to  $C$ ;  $VFA$  is Voids Filled with Asphalt;  $K_a$  is a correction factor, which relates to the thickness  
 126 of asphalt mixture,  $H_1$ .  $\varepsilon_a$  is the compressive strain on the top surface of the subgrade layer;  $\varepsilon_t$   
 127 is the tensile strain on the lower surface of the As layer.

128  $\varepsilon_a$  and  $\varepsilon_t$  are determined through multi-layers model, which involves elastic moduli ( $E$ ) and  
 129 Poisson's ratio ( $\nu$ ) of each layer, built in General Analysis of Multi-layered Elastic Systems  
 130 (GAMES) [Maina and Matsui, 2004] as shown in Fig 1. In present Japanese pavement design  
 131 method, elastic moduli of As layer ( $E_1$ ) changes with temperature as shown in Eqs. (14) and  
 132 (15), while the elastic moduli of base layer ( $E_2$ ) and subgrade layers ( $E_3$ ) are constant through-  
 133 out a whole year since lacking investigation of how water content, freeze-thaw, or stress states  
 134 influence  $E_2$  and  $E_3$ .

$$135 \quad E_1 = -278.4M_p + 10930 \quad (14)$$

$$136 \quad M_p = M_a \left[ 1 + \frac{2.54}{h_1 + 10.16} \right] - \frac{25.4}{9(h_1 + 10.16)} + \frac{10}{3} \quad (15)$$

137 where  $M_p$  is the monthly mean temperature of asphalt mixture at depth of  $h_1$  ( $^{\circ}\text{C}$ );  $M_a$  is monthly  
 138 mean air temperature ( $^{\circ}\text{C}$ );  $h_1$  is the depth equals to one-third of the height of asphalt mixture  
 139 (cm).

140 Consequently, monthly representative  $E_1$  and constant  $E_2/E_3$  are used to calculate allowable



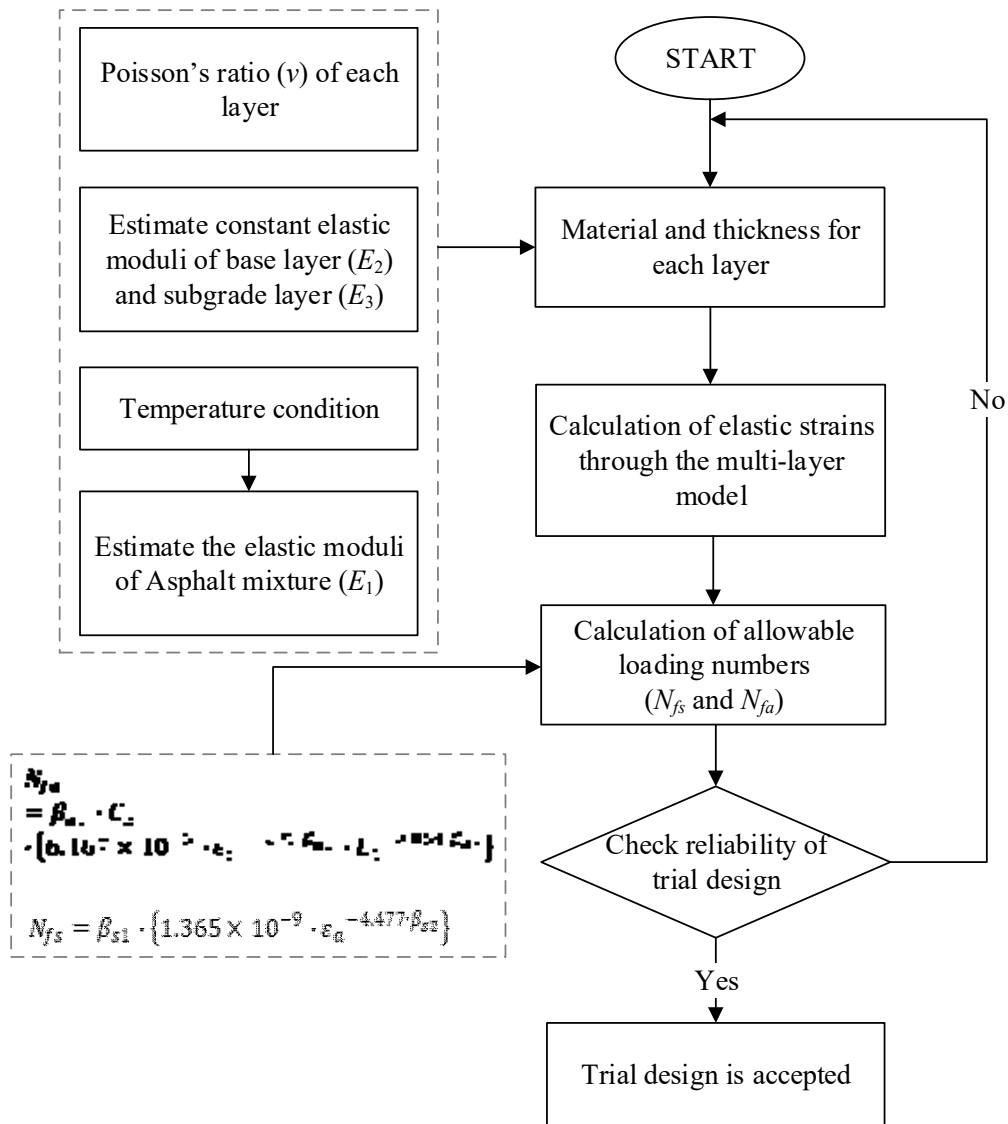
141 loading number under monthly average temperature condition,  $N_{fs,i}$  and  $N_{fa,i}$ .  $i=1\sim 12$ . Failure

142 loading number  $N_{fs,d}$  or  $N_{fa,d}$  is calculated through Eqs. (16) and (17).

143 
$$N_{f,d} = \frac{1}{D_a} \tag{16}$$

144 
$$D_a = \frac{1}{12} \sum_{i=1}^{12} \frac{1}{N_{f,i}} \tag{17}$$

145 As a result, Fig. 2 illustrates the sequence in current Japanese flexible pavement design guide.



146

147 Fig. 2 Sequence in current Japanese flexible pavement design guide.

148 2.2 Test pavement structures

149 Civil Engineering Research Institute for Cold Region (CERI) designed and constructed eight

150 test pavements in Hokkaido [Maruyama et al., 2006]. Fig. 3 illustrates the structures and length

151 of each test pavement. All eight pavement structures consist of asphalt mixture, base layer, and  
 152 subgrade layer with multiple materials and thickness. Four types of hot mixed asphalt mixtures  
 153 are used in test pavement. Fine-graded asphalt mixture has a 0 - 13 mm aggregate gradation  
 154 distribution (hydrated lime, sea sand, and crushed rock). Middle-graded asphalt mixture has the  
 155 same range of gradation distribution but more coarse aggregate. Coarse-graded and stabilized  
 156 asphalt mixture have a 0 - 20 mm and 0 - 30 mm gradation distribution separately. Two types  
 157 of base layer material (Andesite) are used as C-40, crusher-run with maximum 40 mm gradation  
 158 distribution, and C-80, anti-frost crusher-run with maximum 80 mm gradation distribution. The  
 159 subgrade material is a sandy soil according to Unified Soil Classification System [ASTM, 2011],  
 160 named as Tomakomai soil, composed of 8% clay, 13% silt, 51% sand, 28% gravel.

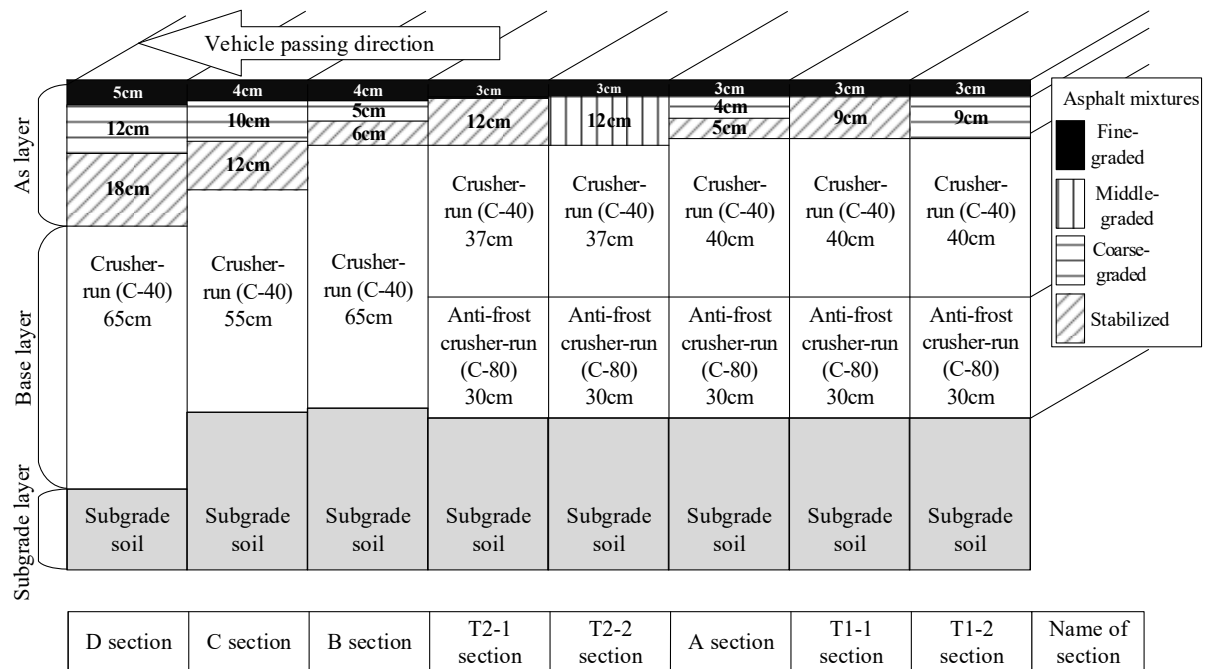


Fig. 3 Test pavement structures.

### 2.3 Traffic volume observation

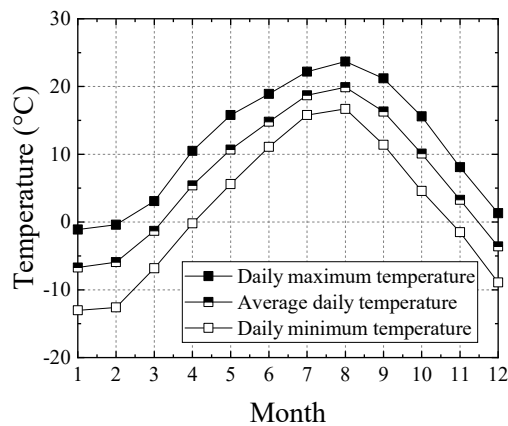
CERI observed traffic volume of test pavement during the whole life (from 1990 to 2004). Total

traffic volume, that is average annual daily vehicle (car and truck) number in one lane, is 4974

166 per day per lane. Truck volume, that is average annual daily truck number in one lane, is 1714  
167 per day per lane. Wheel loads for all vehicles are in accordance with the normal distribution  
168 that ranges from 15 to 80 kN. As Japanese pavement design method calculates the allowable  
169 number of equivalent 49-kN wheel loads against rutting and fatigue cracking. CERI transferred  
170 the traffic volume to a 49-kN wheel loads number as 2398 per day per lane during the whole  
171 life of test pavement.

## 172 2.4 Climate data

173 Climate data are collected from Automated Meteorological Data Acquisition System (AMe-  
174 DAS) [Japan Meteorological Agency]. Fig. 4 plots the monthly average value of daily temper-  
175 atures during the whole life from 1990 to 2004. These climate data are used to determine the  
176 stiffness of the asphalt layer in current Japanese pavement design method through Eqs. (14)  
177 and (15). Besides, the monthly representative temperature is also used in modified design  
178 method to determine the frost-penetration depth, which highly relates to the stiffness of base  
179 and subgrade layer as frozen soil has a much larger stiffness. Determination of variant base and  
180 subgrade layer stiffness related to climate condition will be introduced in latter part.



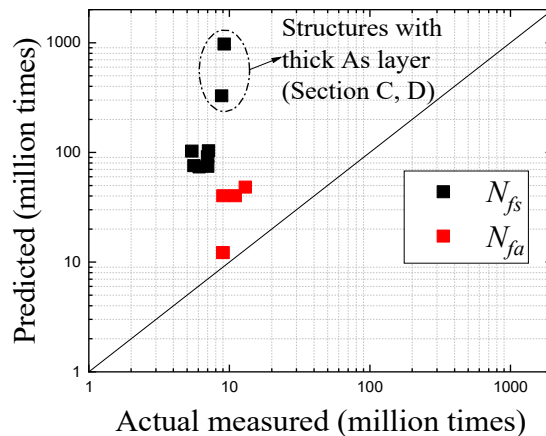
181

182

Fig. 4 Monthly average value of daily temperatures.

183 2.5 Predicted life with present Japanese pavement design method

184 To predict the life of eight test pavements, all test pavements are simplified to three-layers  
185 model in GAMES with layer thickness shown in Fig. 3.  $E_1$  is determined through Eqs. (14) and  
186 (15) and monthly representative air temperatures shown in Fig. 4. Constant stiffness of base  
187 layer ( $E_2$ ) and subgrade layer ( $E_3$ ) through the year is set as 265MPa and 76 MPa referring to  
188 previous research [Maruyama et al., 2008]. Poisson's ratio of As layer, base layer, and subgrade  
189 layer are set as 0.35, 0.35, and 0.4 separately, which come from Japanese pavement design  
190 method recommend values. Fig. 5 compared predicted  $N_{fs}$  and  $N_{fa}$  through Eqs. (3) to (5) and  
191 (6) to (13) with actual measured failure loading number. From Fig.5, it is recognized that, pre-  
192 sent AI model over-estimates the pavement life, especially pavement life against rutting. Be-  
193 sides, prediction bias is much larger for pavement structures with thick As layer refer to two  
194 dots circled by dash line in Fig. 5. Such over-estimation is attributed to the drawbacks of Japa-  
195 nese pavement design method discussed in Introduction part.



196

197 Fig. 5 Predicted pavement life through present Japanese pavement design method.

198 **3. Resilient modulus under various climate conditions and different stress states**

199 3.1 Climate effect on resilient modulus

200 3.1.1 Water content fluctuation

201 Climate effect in this study refers to the synergistic effect between water content and freeze-  
202 thaw action on the resilient modulus of base course and subgrade materials and pavement life.

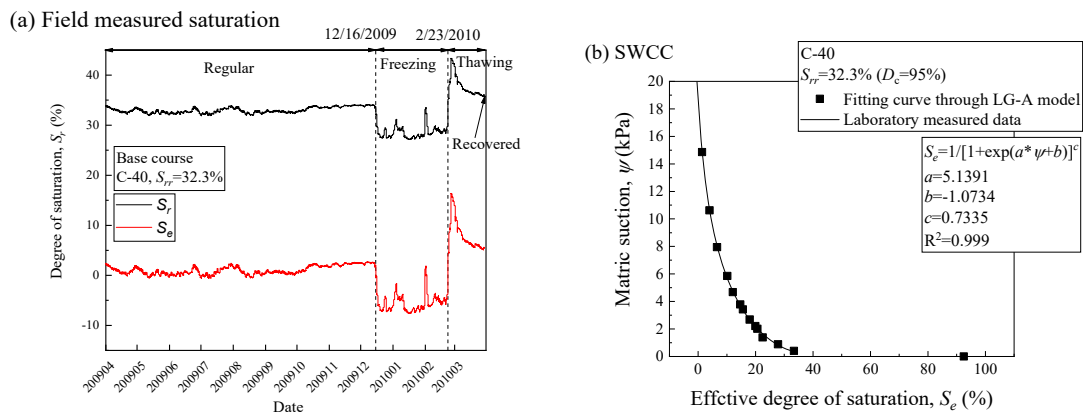
203 The universal model (Eq. (1)) cannot reflect the effect of water content. To overcome such  
204 shortcoming, several modified models [Cary and Zapata, 2011; Liang et al., 2008; Ng et al.,  
205 2013] are proposed based on the universal model to capture the effect of water content on re-  
206 siliant modulus. Within these models, Ng model shown in Eq. (18) adds an independent stress  
207 state variable that incorporates matric suction effects into the universal model and shows good  
208 applicability on predicting resilient modulus of unsaturated unbound granular materials through  
209 the relatively higher coefficient of determination ( $R^2$ ) value than other models [Han and Vana-  
210 palli, 2016]. Monthly representative  $E_2$  and  $E_3$  are estimated through Ng model (Eq. (18)), field-  
211 measured data of water content, and SWCC of base course material and subgrade material.

$$212 \quad M_r = k_1 p_a \left( \frac{\theta}{p_a} \right)^{k_2} \left( \frac{\tau_{oct}}{p_a} + 1 \right)^{k_3} \left( \frac{\psi}{\sigma_{net}} + 1 \right)^{k_4} \quad (18)$$

213 where  $k_1, k_2, k_3, k_4$  are regression constants;  $p_a$  is atmospheric pressure and set as 101 kPa;  $\theta$  is  
214 bulk stress;  $\tau_{oct}$  is octahedral shear stress;  $\sigma_{net}$  is net mean stress (kPa), defined as  $[\theta/3 - u_a]$ ;  $\psi$  is  
215 matric suction (kPa).

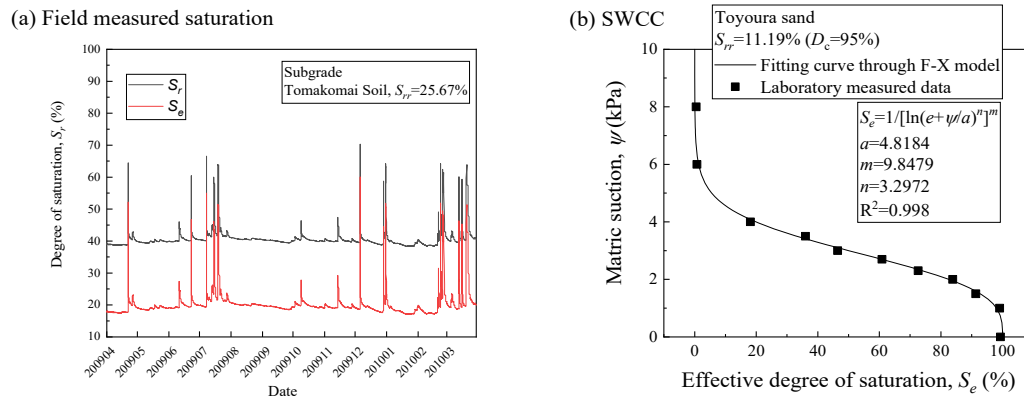
216 Matric suction,  $\psi$  in Eq. (18), is determined by combining SWCC and measured long-term field  
217 measurement of degree of saturation. SWCC of C-40, composed material for base layer, and  
218 long-term field measured water content of base layer are plotted in Fig. 6. The effective degree  
219 of saturation,  $S_e$ , of base layer illustrated as the red line in Fig. 6 (a) was calculated by using a  
220 residual degree of saturation,  $S_{rr}$ , of 32.3%, which was determined through the SWCC measured

221 in laboratory water retentivity test and LG-A model [Mori et al., 2009]. Monthly average  $S_e$  is  
 222 selected to determine monthly matric suction of base layer. Then, monthly representative  $E_2$  is  
 223 estimated with these monthly matric suction values. It is noted that  $S_r$  during freezing season is  
 224 lower than residual  $S_r$  and  $S_e$  during freezing season is consequently lower than zero. This is  
 225 due to functional features of the soil moisture sensor used in the measurement. For this reason,  
 226 unrealistic measured low water content during freezing season is not used. The water content  
 227 just before freezing is used as representative water content for freezing season.



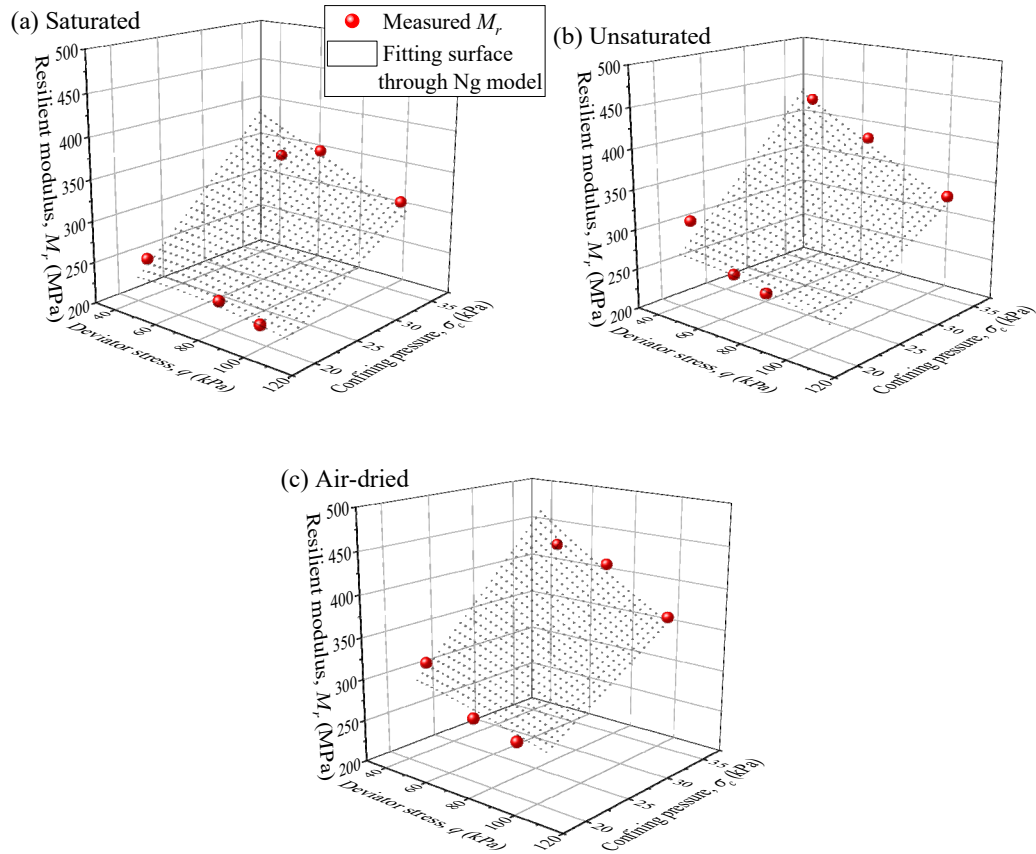
228  
 229 Fig. 6 (a) Long-term field measurement of base layer water content and (b) SWCC of C-40.  
 230 For subgrade layer, it is composed of Tomakomai soil. As the mechanical properties like resil-  
 231 ient modulus of Tomakomai soil is under investigation and the test method of suction-controlled  
 232 freeze-thaw MR test still needs verification, this study uses Toyoura sand, the standard test  
 233 material, to verify newly developed test method and represent the subgrade material to check  
 234 the climate effect on pavement life. It is assumed that effective degree of saturation,  $S_e$ , would  
 235 be same in Toyoura sand subgrade and Tomakomai soil subgrade under same climate condition.  
 236  $S_e$  of subgrade layer illustrated as the red line in Fig. 7 (a) was calculated by using a residual  
 237 degree of saturation ( $S_{rr}$ ) of 25.67%, which was determined through the SWCC estimated with  
 238 grain-size distribution of Tomakomai soil [Fredlund et al., 2002]. Consequently, monthly

239 average  $S_e$  is selected to determine matric suction,  $\psi$  in Eq. (18), of subgrade layer in each  
 240 month through laboratory measured SWCC of Toyoura sand and fitting curve through Fred-  
 241 lund-Xing model [Fredlund and Xing, 1994].



242  
 243 Fig. 7 (a) Long-term field measurement of subgrade layer water content and (b) SWCC of  
 244 Toyoura sand.

245 The value of constants,  $k_1$  to  $k_4$ , in Ng model (Eq. (18)) are determined through regression  
 246 analysis on resilient modulus test results of C-40 and Toyoura sand with variant water contents.  
 247 Resilient modulus of C-40 with three water contents, air-dried ( $S_r=8.2\%$ ), unsaturated  
 248 ( $S_r=36.7\%$ ), saturated ( $S_r=100\%$ ), are determined through medium-size triaxial apparatus.  
 249 More details about the apparatus and test procedure could be found in the previous study [Ishi-  
 250 kawa et al., 2019a]. Resilient modulus of Toyoura sand with two water contents, unsaturated  
 251 ( $S_r=40\%$ ), saturated ( $S_r=100\%$ ), are determined through freeze-thaw triaxial apparatus. More  
 252 details about the apparatus and test procedure could be found in the previous study [Lin et al.,  
 253 2020]. Consequently, Fig. 8 and 9 show the laboratory measured resilient modulus of C-40 and  
 254 Toyoura sand and corresponding fitting surface through Ng model respectively. Table 1 sum-  
 255 marized the value of constants,  $k_1$  to  $k_4$ , in Ng model for C-40 and Toyoura sand.

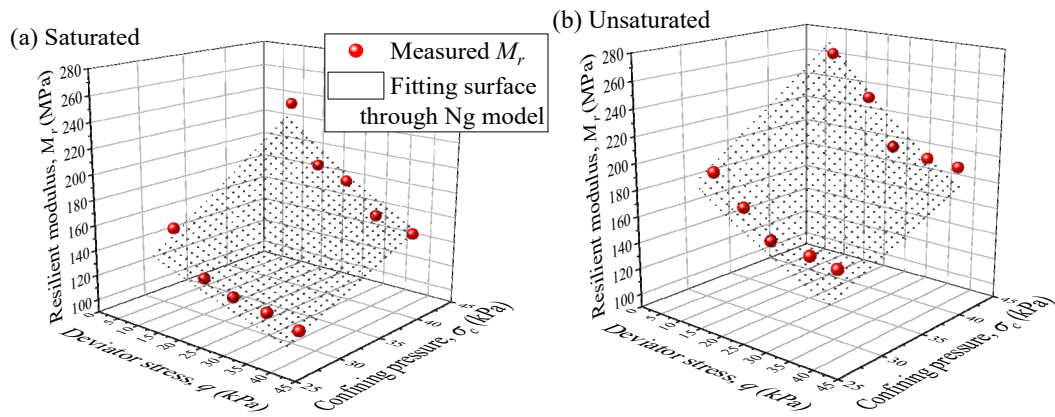


256

257

258

Fig. 8 Resilient modulus of C-40 under different water contents.



259

260

Fig. 9 Resilient modulus of Toyoura sand under different water contents.

261

Table 1. Value of regression constants.

	$k_1$	$k_2$	$k_3$	$k_4$	$R^2$
C-40	3.042	0.886	-1.696	1.076	0.939
Toyouira sand	2.103	1.065	-4.843	2.74	0.949

262

$\theta$ ,  $\tau_{oct}$ , and  $\sigma_{net}$  in Eq. (18) for base layer and subgrade layer are determined with a principal



263 stress ratio equals to 4 under 10 and 5 kPa confining pressure respectively. It is noted that this  
 264 stress condition was selected so that  $M_r$  at normal season matches layer stiffness determined in  
 265 previous research [Maruyama et al., 2008]. Consequently, Table 2 shows the monthly repre-  
 266 sentative base and subgrade layer moduli considering fluctuating water contents estimated  
 267 through Ng model.

268 Table 2 Monthly representative layer moduli considering fluctuating water contents

Name	Elastic moduli (MPa)											
	Jan	Feb	Mar	Apr	May	Jun	Jul	Aug	Sep	Oct	Nov	Dec
Base layer, $E_2$	217	209	143	193	195	195	174	185	195	191	189	208
Subgrade layer, $E_3$	77	75	61	76	76	71	69	76	76	76	76	75

269 3.1.2 Freeze-thaw action

270 When considering the synergistic effect between freeze-thaw action and seasonal fluctuation in  
 271 water content on the stiffness of base and subgrade layer, the monthly representative elastic  
 272 moduli were divided into three types of seasonal  $E$  values ( $E$  for freezing season, thawing sea-  
 273 son, and regular season except for freezing and thawing seasons) for the simplicity of the pave-  
 274 ment life analysis.

275 Since there is no freeze-thaw effect during the regular season, the  $E$  value for the regular season  
 276 is estimated by Ng model as shown in Eq. (18) in a same way introduced in last section.

277 The  $E_2$  and  $E_3$  value for freezing season is set as 600 MPa and 200 MPa separately, according  
 278 to back analysis of FWD test results [Ishikawa et al., 2019a]. In addition, this study assumes  
 279 that when the average frost-penetration depth for the month gets into the base or subgrade layer  
 280 regardless of deep or shallow, the  $E$  increases due to freezing. Here, the average frost-penetra-  
 281 tion depth ( $z$ ) was calculated by substituting the freezing index calculated from the daily mean  
 282 air temperatures measured by AMeDAS into the modified Berggren formula [Aldrich Jr, 1956]

283 shown below:

$$284 \quad z = \alpha \sqrt{\frac{172800F}{(L/\lambda)_{eff}}} \quad (19)$$

285 where  $\alpha$  is a correction coefficient;  $F$  is a freezing index which is the average air temperature  
286 during freezing season multiplied by its duration in days;  $(L/\lambda)_{eff}$  is an effective ratio of  $L$  to  $\lambda$ ;  
287  $L$  is the latent heat of soil;  $\lambda$  is a thermal conductivity of the soil.

288 The  $E$  value for thawing season stands for the average value between the moduli just after  
289 thawing, corresponds to the highest water content during thawing season, and the moduli at the  
290 end of thawing season, corresponds to the lowest water content during thawing season. The  $E$   
291 value during thawing season is estimated by modified Ng model (Eq. (20)), which is proposed  
292 by Lin et al. [2020], with considering climate effect,  $F_{clim}$ . By adding new parameter  $F_{clim}$  into  
293 Ng model as shown in Eq. (20), modified Ng model captures the complex climate effect. The  
294  $E$  value at the end of thawing season is estimated through Eq. (18) since the effect of freeze-  
295 thaw is excluded.

$$296 \quad M_r = F_{clim} \cdot k_1 \cdot p_a \left(\frac{\theta}{p_a}\right)^{F_{clim} \cdot k_2} \left(\frac{\tau_{oct}}{p_a} + 1\right)^{F_{clim} \cdot k_3} \left(\frac{\psi}{\sigma_{net}} + 1\right)^{F_{clim} \cdot k_4} \quad (20)$$

297 Except modified Ng model, Liang model [Liang et al., 2008] is another approach to estimate  
298 resilient modulus with changing stress states like bulk stress, octahedral shear stress, and matric  
299 suction. Eqs (21) and (22) show the Liang model. The most difference between Liang model  
300 and Ng model is that the former one incorporates the matric suction into applied bulk stress,  
301 while the latter one extends the independent stress state variable. To capture the freeze-thaw  
302 effect on resilient modulus, Ishikawa et al. [2019a] modified Liang model (Eq. (23)) is built by  
303 adding a reduction factor,  $f(N_f, \theta)$ , on Eq. (21).  $f(N_f, \theta)$  uses number of freeze-thaw process cycles  
304 ( $N_f$ ) and volumetric water content ( $\theta$ ) for the sample as explanatory variables.

305 
$$M_R = k_1 p_a \left( \frac{\theta_b + \chi \psi}{p_a} \right)^{k_2} \left( \frac{\tau_{oct}}{p_a} + 1 \right)^{k_3} \quad (21)$$

306 
$$\chi = \left( \frac{(u_a - u_w)_b}{\psi} \right)^{0.55} \quad (22)$$

307 
$$M_R = f(N_f, \theta) \cdot k_1 p_a \left( \frac{\theta_b + \chi \psi}{p_a} \right)^{k_2} \left( \frac{\tau_{oct}}{p_a} + 1 \right)^{k_3} \quad (23)$$

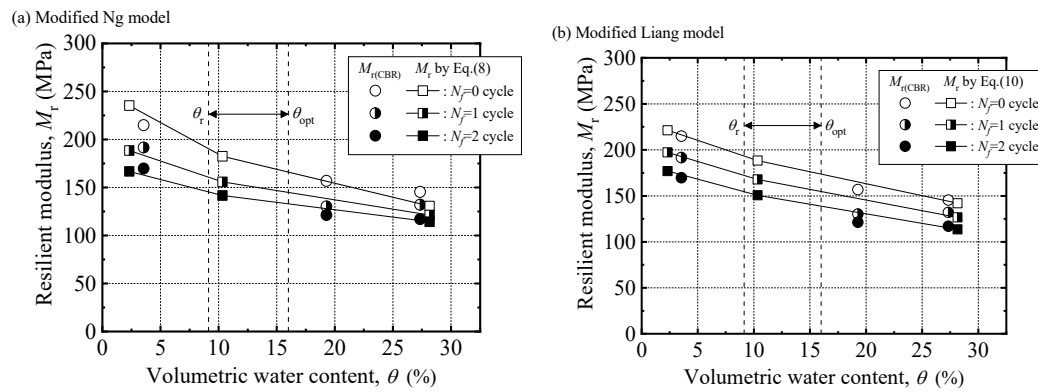
308 where  $\theta_b$  is bulk stress;  $(u_a - u_w)_b$  is air entry value.

309 For base course material, both Ng model (Eq. (18)) and Liang model (Eq. (21)) have high R<sup>2</sup>  
310 value on the unfrozen C-40 material as shown in Table 3. The applicability of modified Ng  
311 model (Eq. (20)) and modified Liang model (Eq. (23)) on freeze-thawed C-40 are checked by  
312 comparing estimated  $M_r$  with freeze-thawed  $M_{r(CBR)}$ . Freeze-thawed  $M_{r(CBR)}$  is detected with a  
313 freeze-thaw CBR (California Bearing Ratio) test apparatus which is based on a general CBR  
314 test apparatus and improved to reproduce in a laboratory environment the freeze-thaw history  
315 expected to be applied to the base course materials in the in-situ pavement structures. A series  
316 of freeze-thaw CBR tests for C-40 was conducted under three different water contents, air-dried  
317 ( $S_r=12.3\%$ ), unsaturated ( $S_r=67\%$ ), saturated ( $S_r=95\%$ ), along with three different patterns of  
318 freeze-thaw history, no freeze-thaw, once freeze-thaw, and twice freeze-thaw, in order to exam-  
319 ine the effects of freeze-thaw action and water content on the frost-heave and bearing-capacity  
320 characteristics of base course material. More details about the freeze-thaw CBR test apparatus  
321 and procedure could be found in the previous study [Ishikawa et al., 2019a]. Fig. 10 shows the  
322  $M_{r(CBR)}$  and estimated  $M_r$  with Eq. (20) and (23). It is noted that, both models can give reason-  
323 able predicted  $M_r$  and also capture the decreasing  $M_r$  with more freeze-thaw numbers and higher  
324 water contents. Table 3-1 also shows the R<sup>2</sup> value,  $F_{clim}$ , and  $f(N_f, \theta)$  of modified Ng model (Eq.  
325 (20)) and modified Liang model (Eq. (23)) on freeze-thawed  $M_{r(CBR)}$ . It is noted that when con-  
326 ducting regression analysis for freeze-thawed test, only  $F_{clim}$  and  $f(N_f, \theta)$  are variant and  $k_1$  to  $k_4$

327 are fixed to check the validity of newly added parameters. Both models show high accuracy  
 328 ( $R^2 > 0.9$ ).

329 Table 3. Applicability of Modified Liang model and Modified Ng model on C-40

		$k_1$	$k_2$	$k_3$	$k_4$	$F_{clim}$	$f(N_f, \theta)$	$R^2$
U	Ng model	3.042	0.886	-1.696	1.076	—	—	0.939
	Liang model	4.861	1.525	-2.092	—	—	—	0.950
FT ( $N_f=1$ )	modified Ng model	3.042	0.886	-1.696	1.076	0.749	—	0.921
	modified Liang model	4.861	1.525	-2.092	—	—	0.891	0.991
FT ( $N_f=2$ )	modified Ng model	3.042	0.886	-1.696	1.076	0.644	—	0.968
	modified Liang model	4.861	1.525	-2.092	—	—	0.800	0.998



330

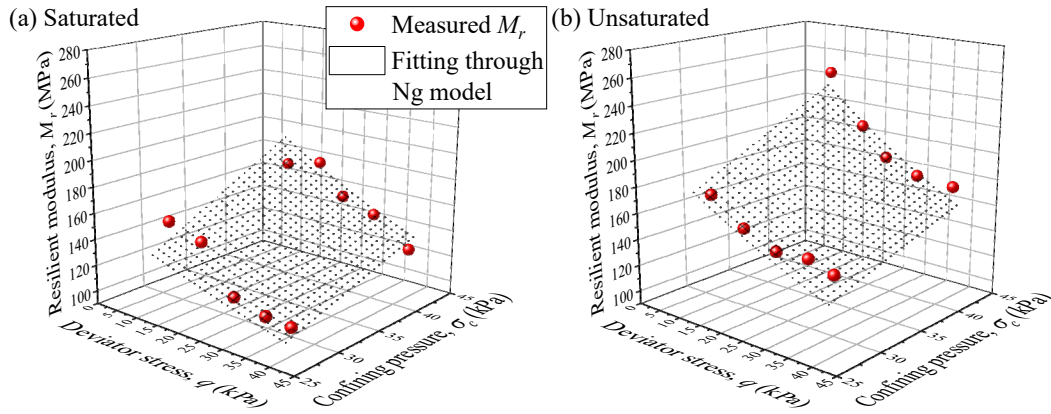
331 Fig. 10 Estimated  $M_r$  with (a) modified Ng model and (b) modified Liang model.

332 For subgrade material, Table 4 shows the applicability of Ng model (Eq. (18)) and Liang model  
 333 (Eq. (21)) on unfrozen Toyoura sand, and the applicability of modified Ng model (Eq. (20))  
 334 and modified Liang model (Eq. (23)) on freeze-thawed Toyoura sand. Freeze-thaw resilient  
 335 modulus of Toyoura sand is detected with freeze-thaw triaxial apparatus which could circulate  
 336 low temperature fluids in the cap, pedestal, and inner cell to control the cap, pedestal, and  
 337 around temperature of specimen separately to simulate one-dimensional freeze-thaw action. A  
 338 series of freeze-thaw resilient modulus tests for Toyoura sand was conducted under two differ-  
 339 ent water contents, unsaturated ( $S_r=40\%$ ), saturated ( $S_r=100\%$ ), along with two different pat-  
 340 terns of freeze-thaw history, no freeze-thaw and once freeze-thaw, in order to examine the ef-  
 341 fects of freeze-thaw action and water content on the mechanical properties of subgrade

342 materials. More details about the test condition and results could be found in previous research  
 343 [Lin et al., 2020]. Fig. 11 shows the freeze-thaw resilient modulus test results for Toyoura sand.  
 344 It is noted that unfrozen resilient modulus test results for Toyoura sand is already plotted in Fig.  
 345 9.

346 Table 4. Applicability of Modified Liang model and Modified Ng model on Toyoura sand

		$k_1$	$k_2$	$k_3$	$k_4$	$F_{clim}$	$f(N_f, \theta)$	$R^2$
U	Ng model	2.103	1.065	-4.843	2.74	—	—	0.949
	Liang model	2.396	0.979	-4.912	—	—	—	0.767
FT ( $N_f=1$ )	modified Ng model	2.103	1.065	-4.843	2.74	0.885	—	0.901
	modified Liang model	2.396	0.979	-4.912	—	—	0.910	0.621



347  
 348 Fig. 11 Freeze-thaw resilient modulus of Toyoura sand under different water contents.  
 349 When performing regression analysis for freeze-thaw test results through modified Ng model  
 350 (Eq. (10)) or modified Liang model (Eq. (12)), only  $F_{clim}$  and  $f(N_f, \theta)$  are variant and  $k_1$  to  $k_4$  are  
 351 fixed to the same value obtained from regression analysis on unfrozen test results to check the  
 352 validity of newly added parameters. It is recognized that Ng model shows much higher  $R^2$  value  
 353 than Liang model no matter for unfrozen or freeze-thawed C-40 and Toyoura sand. Conse-  
 354 quently, this study uses modified Ng model to estimate resilient modulus of base layer and  
 355 subgrade layer with fluctuating water content and various freeze-thaw histories. In addition,  
 356 Table 5 shows the monthly representative base and subgrade layer moduli estimated through

357 modified Ng model with considering fluctuating water contents and freeze-thaw action.  
 358 Through comparing Table 2 and 5, it is concluded the  $M_r$  increases to a high value during freez-  
 359 ing season and drops further in thawing season according to the thaw weakening no matter for  
 360 base or subgrade layer.

361 Table 5 Monthly representative layer moduli considering climate effect

Name	Elastic moduli (MPa)											
	Jan	Feb	Mar	Apr	May	Jun	Jul	Aug	Sep	Oct	Nov	Dec
Base layer, $E_2$	600	600	110	193	195	195	174	185	195	191	189	208
Subgrade layer, $E_3$	77	200	50	76	76	71	69	76	76	76	76	75

362 3.2 Dependency of resilient modulus on stress state

363 As discussed in introduction part, present Japanese design guide use constant elastic moduli of  
 364 base layer and subgrade layer to calculate the strains under 49-kN wheel load. To overcome the  
 365 limitation that unchangeable layer moduli under variant stress states caused by different layer  
 366 thickness, the widely used resilient modulus in MEPDG, which changes with different stress  
 367 states like deviator stress and confining pressure, is applied in this study to estimate the layer  
 368 stiffness precisely. A convergence analysis of  $M_r$  is necessary to determine the reliable layer  
 369 stiffness under 49-kN wheel loads since  $M_r$  affects and is conversely affected by the stress states.

370 The convergence analysis is conducted through following steps [JSCE 2015]:

- 371 1) Input  $E_1$ ,  $E_2^I$ , and  $E_3^I$  in the GAMES to obtain the stress states in base layer and subgrade  
 372 layer. According to previous researches [Huang, 2004], stress states in two points shown in Fig.  
 373 12 are chosen to estimate  $E$  for whole base and subgrade layer.

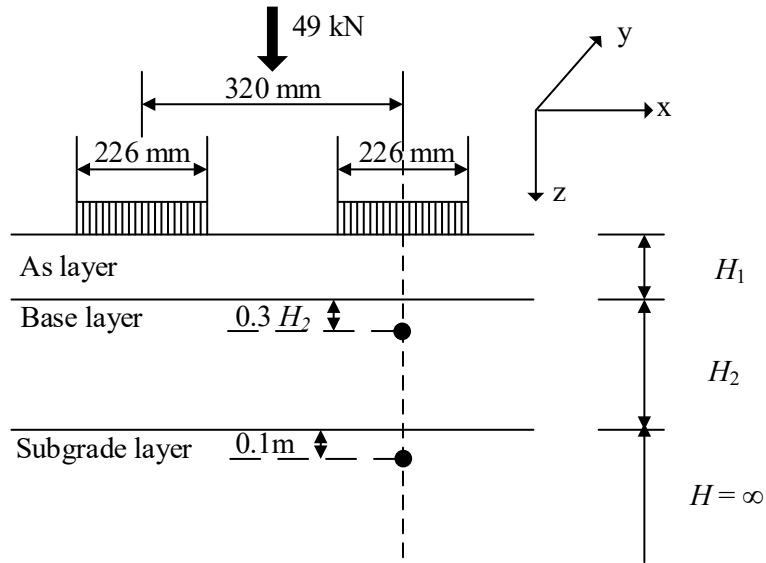


Fig. 12 Stress states calculation points in base and subgrade layer.

2) Substitute the stress states obtained in step 1 into modified Ng model to obtain new  $E_2^2$  and

$E_3^2$ .

3) Step 1 and 2 are repeated until the error calculated in following equation is less than 1%.

$$e_{rr} = \frac{|E^{i-1} - E^i|}{E^i} \times 100 \quad (24)$$

where  $E^i$  and  $E^{i-1}$  is the layer modulus estimated in  $i$  th and  $i-1$ th iterations.

Based on this convergence analysis sequence, Fig. 13 shows the development of estimated re-

silient modulus of base layer and subgrade layer with number of iterations in normal season

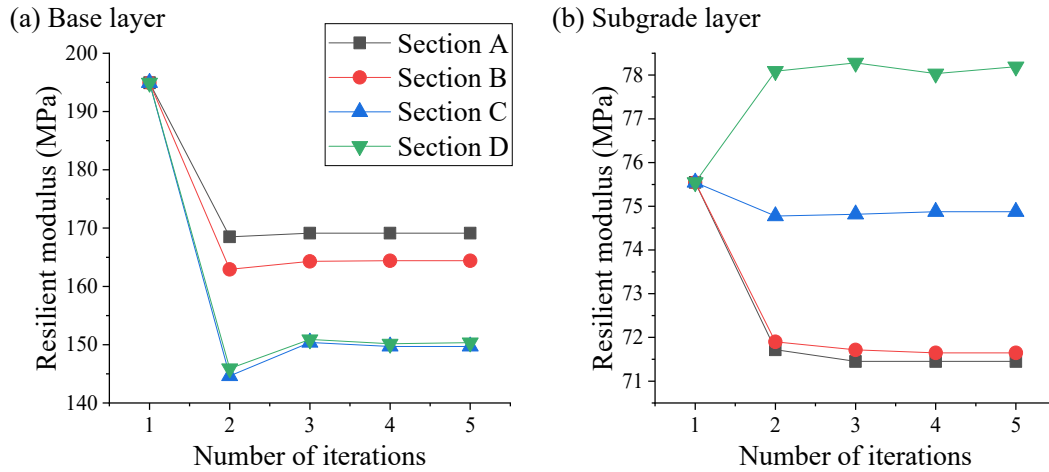
(Aug). It is noted that all moduli are stable after 2-4 iterations. Besides, convergent  $E_2$  decreases

in all pavement sections and convergent  $E_3$  decreases in section A, B, C while increases in

section D compared with elastic moduli without convergence analysis. Resilient moduli in other

month show similar tendency that  $E_2$  decreases in all pavement sections and  $E_3$  decreases in

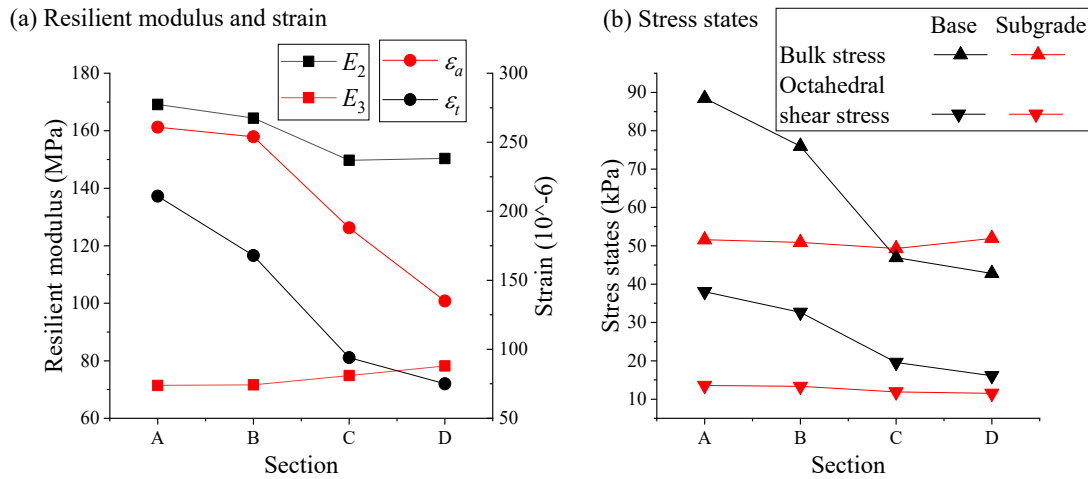
section with thin As layer while increases in section with thick As layer.



388

389

Fig. 13 Estimated resilient modulus of (a) base layer and (b) subgrade layer.



390

391

Fig. 14 (a) Resilient modulus and (b) stress states in different sections.

392 Different increasing or decreasing tendency comes from the variant stress states when pavement  
 393 structures changing. To clearly discuss how pavement structures and stress states influence the  
 394 resilient modulus at stable condition, Fig. 14 compares resilient modulus, strain, and stress  
 395 states in different sections. Since As layer thickness increases from section A to D, it is con-  
 396 cluded that  $E_2$  decreases significantly with As layer thickness while  $E_3$  slightly increases with  
 397 As layer thickness. It is noted that Fig. 14 only show convergent resilient modulus and corre-  
 398 sponding stress sates for Aug, which stands for the normal season, and that resilient modulus  
 399 and corresponding stress sates for other months show the same tendency. Such tendency could



400 be attributed to the changing bulk stress ( $\theta$ ) and octahedral shear stress ( $\tau_{oct}$ ) with As layer  
401 thickness, as shown in Fig 14 (b).  $\theta$  has a positive effect on the  $M_r$  while  $\tau_{oct}$  has a negative  
402 effect. In base layer, decreasing  $\theta$  with thicker As layer is more significant than decreasing  $\tau_{oct}$   
403 with thicker As layer. Consequently,  $E_2$  decreases from A to D. In subgrade layer,  $\theta$  increases  
404 while  $\tau_{oct}$  decreases with As layer thickness. As a result,  $E_3$  increases from A to D. Since fluctua-  
405 tion of stress states in base layer is much significant than those in subgrade layer, fluctuation  
406 of moduli in base layer is accordingly larger. Elastic strains ( $\varepsilon_a$  and  $\varepsilon_t$ ) are also shown in Fig. 14  
407 (a). It is clear that no matter compressive strain ( $\varepsilon_a$ ), which is used in Eq. (1) to calculate  $N_{fs}$ , or  
408 tensile strain ( $\varepsilon_t$ ), which is used in Eq. (4) to calculate  $N_{fa}$ , both strains decrease with As layer  
409 thickness. Such tendency is reasonable as asphalt mixture has a much larger stiffness than  
410 crusher-run material and subgrade soil, and a thicker As layer improves the mechanical prop-  
411 erties of the whole multi-layer elastic structure. Table 6 summarizes the convergent monthly  
412 representative base/subgrade layer moduli in A section.  $M_r$  for freezing season keeps constant  
413 due to freezing of soils. In this case, this study only performs the convergence analysis again  
414  $M_r$  except the freezing season.

415 Table 6 Convergent monthly representative base/subgrade layer moduli in A section.

Name	Elastic moduli (MPa)											
	Jan	Feb	Mar	Apr	May	Jun	Jul	Aug	Sep	Oct	Nov	Dec
$E_2$ -Water con- tent fluctua- tion	191	185	132	173	175	175	161	169	176	172	170	184
$E_2$ -Climate ef- fect	600	600	105	173	175	175	161	169	176	172	170	184
$E_3$ -Water con- tent fluctua- tion	74	73	58	74	73	69	68	72	73	73	73	73
$E_3$ -Climate ef- fect	77	200	40	74	73	69	68	72	73	73	73	73

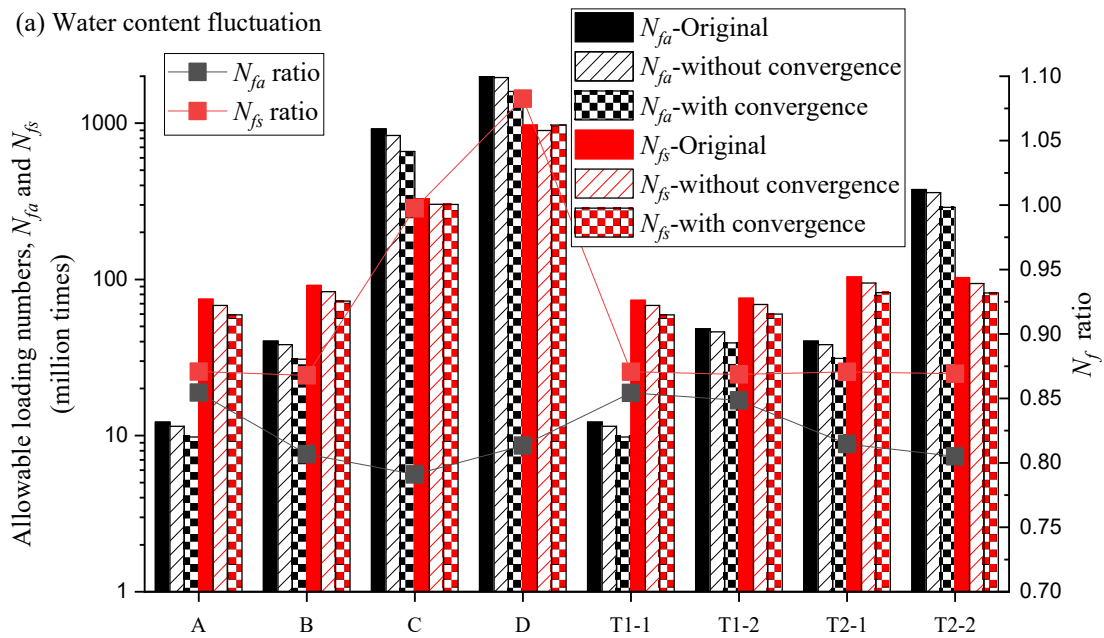
### 416 3.3 Influence of stress state and climate effect on pavement life

#### 417 3.3.1 Stress state dependency

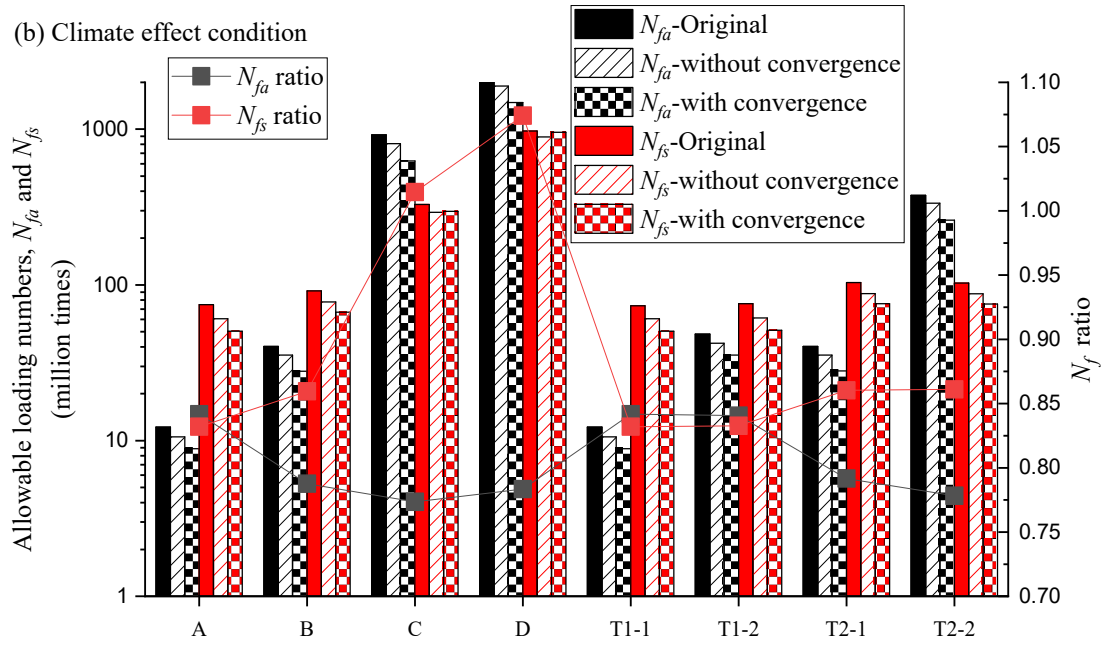
418 Fig.15 illustrates the calculated pavement life of all sections through layer moduli with and  
419 without convergence analysis. The ratio of  $N_f$  with convergent  $E_2$  and  $E_3$  to  $N_f$  without conver-  
420 gent  $E_2$  and  $E_3$  is also plotted here. Pavement life under water content fluctuation condition,  
421 which means layer stiffness  $E_2$  and  $E_3$  changing with water contents, and climate condition,  
422 which means  $E_2$  and  $E_3$  changing with water contents and freeze-thaw action, are shown in  
423 Figs.15 (a) and (b) separately.  $N_{fa}$  always decreases with convergent  $E_2$  and  $E_3$  regardless of  
424 pavement structures while  $N_{fs}$  only decreases with convergent  $E_2$  and  $E_3$  in pavement structures  
425 with thin As layer (A, B, T1 and T2). Convergent  $E_2$  and  $E_3$  has a negative effect on the pave-  
426 ment life against fatigue cracking and this effect is more significant in thick As layer pavement  
427 structure. On the other hand, convergent  $E_2$  and  $E_3$  has a negative effect on the pavement life  
428 against rutting when As layer is thin. Consequently, convergence analysis for layer stiffness is  
429 essential when developing a mathematical flexible pavement design method with high applica-  
430 bility and precision.

431 In addition, the effect of convergence analysis on pavement life is basically more significant  
432 compared with effect of water content fluctuation or climate effect regardless of section struc-  
433 ture. To be precise, the difference between  $N_f$ -Original, the pavement life calculated with con-  
434 stant  $E_2$  and  $E_3$ , and  $N_f$ -without convergence is less significant than the difference between  $N_f$ -  
435 without convergence and  $N_f$ -with convergence no matter the water content fluctuation (Fig.  
436 15(a)) or climate effect is considered (Fig. 15(b)). The only exception that the effect of conver-  
437 gence analysis is less significant than effect of water content fluctuation or climate effect is for

438 the pavement life against rutting ( $N_{fs}$ ) of structure with thick As layer. For example, for section  
 439 C and D, the difference between  $N_{fs}$ -Original and  $N_{fs}$ -without convergence is more significant  
 440 than the difference between  $N_{fs}$ - without convergence and  $N_{fs}$ -with convergence. Such results  
 441 indicate that in pavement structures such as high-standard roads, environmental condition de-  
 442 pendence has a greater effect on pavement life than stress dependence and should be considered  
 443 as a more significant factor. Especially in the case of Japanese pavement where rutting is more  
 444 of a problem than fatigue cracking.



445



446

447 Fig. 15 Convergence analysis effect on pavement life under (a) water content fluctuation con-

448

dition (b) climate effect condition

449

### 3.3.2 Climate effect on pavement life

450

Figs. 16 and 17 illustrate  $N_{fs}$  and  $N_{fa}$  of eight test pavement structures under three conditions,

451

namely Original, Water content fluctuation, and Climate effect. It is noted that all pavement life

452

in water content fluctuation condition and climate condition are calculated with convergent

453

layer moduli. In other words, Figs. 16, 17 are plotted by rearranging the calculation results in

454

Fig. 15. It is obvious that  $N_{fs}$  and  $N_{fa}$  both decrease from original condition to water content

455

condition, which implies that changing  $E_2$  and  $E_3$  with fluctuating water content decrease pave-

456

ment life.  $N_{fs}$  and  $N_{fa}$  decrease further from water content fluctuation condition to climate con-

457

dition, which indicates that freeze-thaw action decreases pavement life further as the decreasing

458

$E_2$  and  $E_3$  during thawing season has a stronger influence on the pavement life than the increas-

459

ing  $E_2$  and  $E_3$  during the freezing season.

460

To clearly discuss the influence of water content fluctuation, freeze-thaw action, and climate

461 effect on the pavement life,  $R_{Nf}$  for different structures are also plotted in the Figs. 16 and 17.

462 The  $R_{Nf}$  considering water content fluctuation or climate effect are determined through dividing

463 the  $N_f$ -Water content fluctuation or  $N_f$ -Climate effect by the  $N_f$ -Original, while the  $R_{Nf}$  consid-

464 ering freeze-thaw action is determined through dividing the  $N_f$ -Climate effect by the  $N_f$ -Water

465 content fluctuation. All ratios are lower than 1, indicates that influence of water content fluctu-

466 ation, freeze-thaw action, and climate effect on  $E_2$  and  $E_3$  all decrease the pavement life. Within

467 pavement life against rutting calculation results,  $R_{Nf}$  caused by water content, freeze-thaw ac-

468 tion, and climate effect are around 0.819, 0.931, and 0.765 separately. In other words, the  $N_{fs}$

469 decreases 18.1% when changing  $E_2$  and  $E_3$  caused by water content fluctuation is considered

470 and it would further decrease 6.9% when effect of freeze-thaw action on  $E_2$  and  $E_3$  is also con-

471 sidered. A synergistic climate effect on  $E_2$  and  $E_3$  decreases  $N_{fs}$  about 23.5%. Within pavement

472 life against fatigue cracking calculation results,  $R_{Nf}$  caused by water content, freeze-thaw action,

473 and climate effect are around 0.759, 0.93, and 0.706 separately. In other words, the  $N_{fa}$  decreases

474 24.1% when changing  $E_2$  and  $E_3$  caused by water content fluctuation is considered and it would

475 further decrease 7% when effect of freeze-thaw action on  $E_2$  and  $E_3$  is also considered. A syn-

476 ergistic climate effect on  $E_2$  and  $E_3$  decreases  $N_{fa}$  about 29.4%. It is noted that, all these decreas-

477 ing ratios include the effect of convergence analysis discussed in previous section.

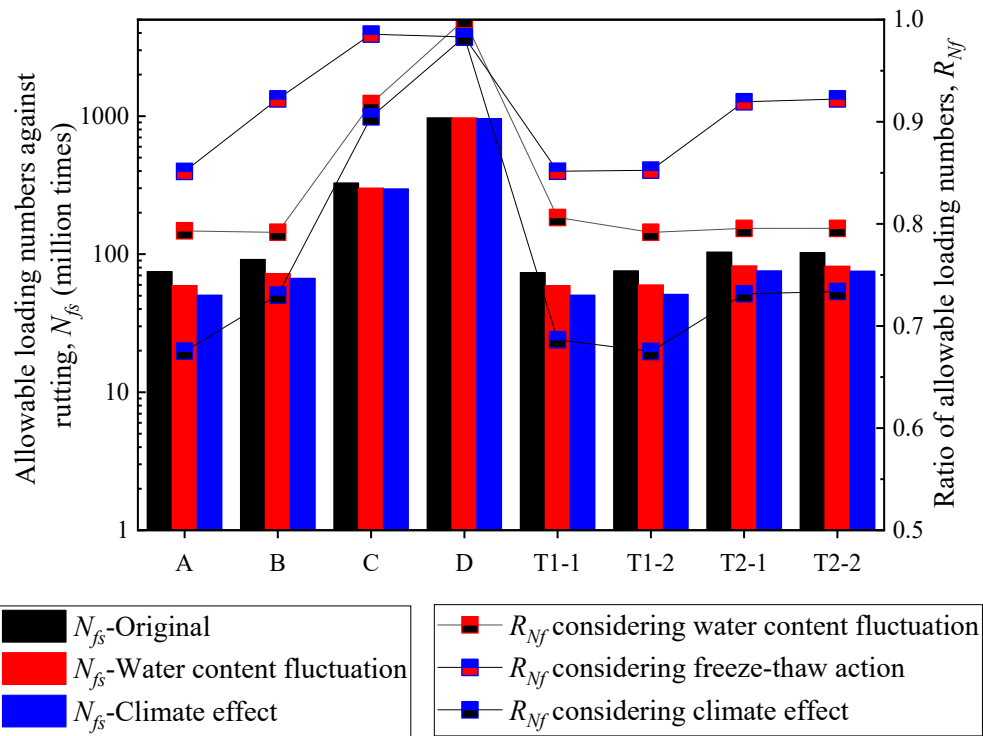
478 These results suggest that for improving the applicability and validity of the current Japanese

479 design standard, the introduction of the theoretical design method for pavement structures,

480 which can take account of the effects of the freeze-thaw actions and the concurrent seasonal

481 fluctuation in water content on the base and subgrade layer stiffness, is effective in the asphalt

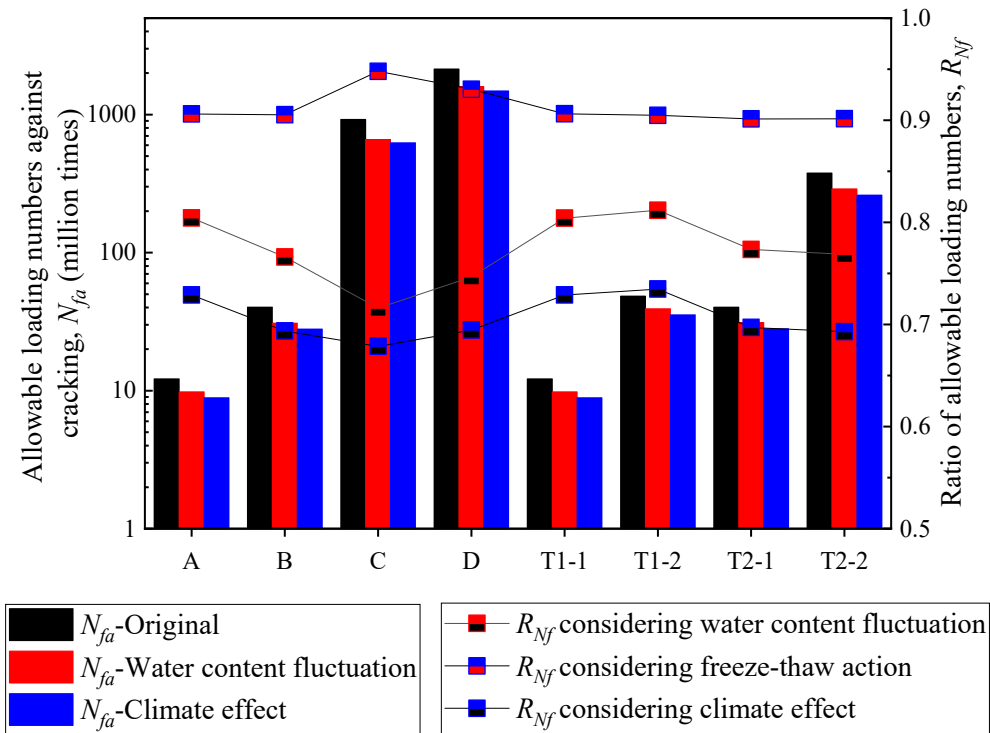
482 pavements for cold regions.



483

484

Fig. 16  $N_{fs}$  of eight test pavement structures.



485

486

Fig. 17  $N_{fa}$  of eight test pavement structures.

487 **4. Modification of failure criteria**

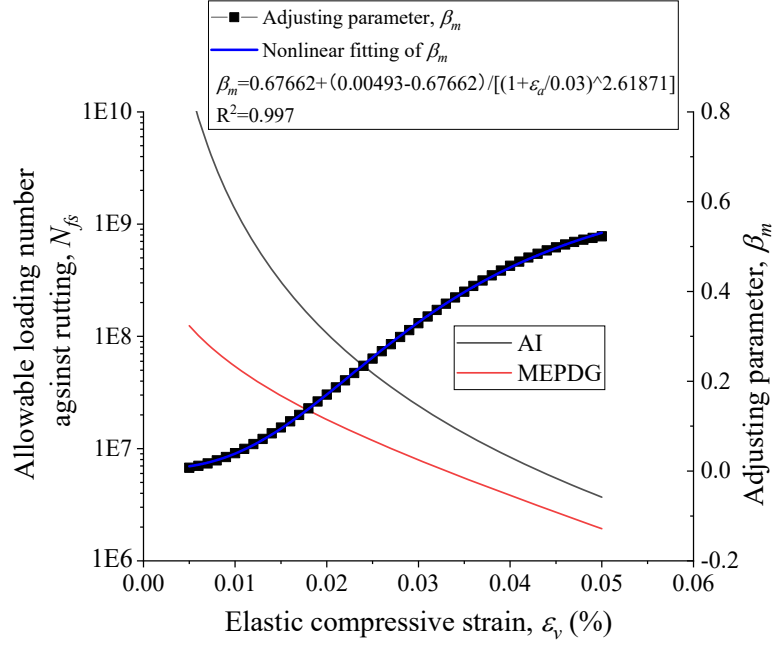
488 4.1 MEPDG rutting prediction model

489 To overcome the limitations of Japanese rutting failure criterion explained in the introduction  
490 part, this section modified the structure of AI model (Eq. (3)) referring to MEPDG rutting depth  
491 prediction model (Eq. (2)).

492 By applying the rutting failure threshold value in present Japanese design guide (15mm) into  
493 Eq. (2), allowable loading number against rutting could be calculated through Eq. (25).

494 
$$N_{fs} = \rho \cdot \left( \ln \left( \frac{\beta_{s1} k_1 \varepsilon_v h \left( \frac{\varepsilon_0}{\varepsilon_r} \right)}{15} \right) \right)^{-1/\beta} \quad (25)$$

495 Fig. 18 shows the allowable loading number against rutting through AI model (namely  $N_{fs}$ -AI)  
496 and MEPDG model (namely  $N_{fs}$ -MEPDG) under various elastic compressive strain ( $\varepsilon_v$ ).  $N_{fs}$ -AI  
497 is much larger than  $N_{fs}$ -MEPDG when  $\varepsilon_a$  locates between 50 to 500 E-6, which is the normal  
498 range for  $\varepsilon_a$ . In other words, AI model greatly overestimate the allowable loading number  
499 against rutting as compared with MEPDG model. To modify the AI model based on MEPDG,  
500 this study introduces an adjusting parameter,  $\beta_m$ , to the traditional AI model. Newly developed  
501 one is named as AI-MEPDG rutting model as show in Eq. (26).  $\beta_m$  is calculated through divid-  
502 ing  $N_{fs}$ -MEPDG by  $N_{fs}$ -AI. A logistic function is used to build the relation between  $\beta_m$  and  $\varepsilon_a$ ,  
503 as shown in Fig. 18 and Eq. (27). Consequently, AI-MEPDG rutting model is shown in Eqs.  
504 (26) and (27) to calculate allowable loading number against rutting.



505

506 Fig. 18 Allowable loading number against rutting calculated through AI and MEPDG model.

507 
$$N_{fs} = \beta_m \cdot \beta_{s1} \cdot \{1.365 \times 10^{-9} \cdot \varepsilon_a^{-4.477 \cdot \beta_{s2}}\} \quad (26)$$

508 
$$\beta_m = A_2 + \frac{A_1 - A_2}{1 + (\varepsilon_a / x_0)^p} \quad (27)$$

509  $A_1$  and  $A_2$ : lower and upper limit of  $\beta_m$  and the  $A_1$  is forced as positive value.  $A_1=0.000493$ ;

510  $A_2=0.67672$ .

511  $x_0$ : fitting parameter, equals to 0.03.

512  $p$ : fitting parameter, equals to 2.61871.

513 With AI-MEPDG rutting model, the  $N_{fs}$  in climate condition is calculated and illustrated in Fig.

514 19. It is noted that,  $N_{fs}$  through AI-MEPDG rutting model in Fig. 19 is calculated with conver-

515 gent layer moduli. The tendency for the ratio of  $N_{fs}$  with convergence to  $N_{fs}$  without convergence

516 in AI-MEPDG rutting model is almost similar to that in Fig. 15. AI-MEPDG rutting model

517 gives much smaller predicted  $N_{fs}$  than AI model predicted value. However, compared with ac-

518 tual measured loading number at failure, predicted  $N_{fs}$  through AI-MEPDG rutting model are

519 still too large. Bias between predicted and actual pavement life are probably caused by



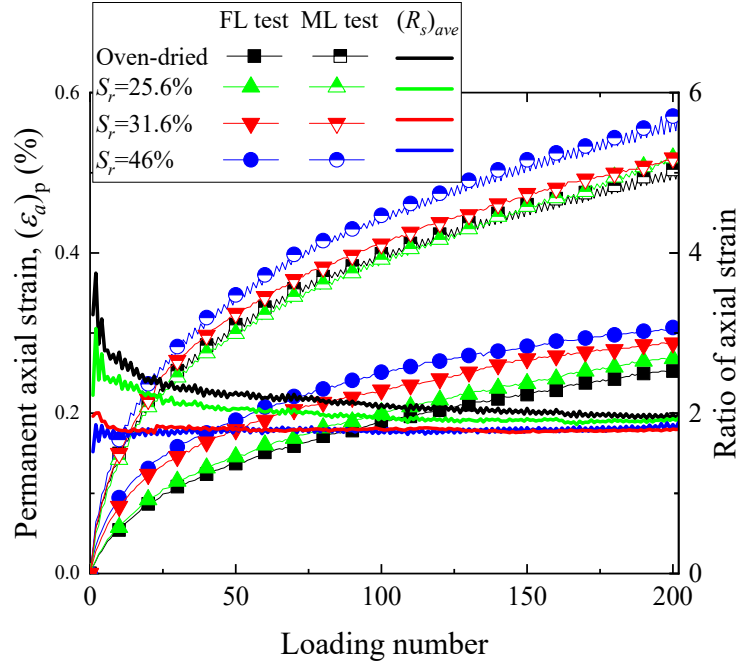


Name	sample	content	Height (mm)	density (g/cm <sup>3</sup> )	axial stress, ( $\sigma_a$ ) <sub>max</sub> (kPa)	shear stress, ( $\tau_{a\theta}$ ) <sub>max</sub> (kPa)
FL	Toyoura sand	Oven-dried	100	1.463	72.58	0
FL	Toyoura sand	$S_r=25.6\%$	100	1.463	72.58	0
FL	Toyoura sand	$S_r=31.6\%$	100	1.463	72.58	0
FL	Toyoura sand	$S_r=46\%$	100	1.463	72.58	0
ML	Toyoura sand	Oven-dried	100	1.463	72.58	18.12
ML	Toyoura sand	$S_r=25.6\%$	100	1.463	72.58	18.12
ML	Toyoura sand	$S_r=31.6\%$	100	1.463	72.58	18.12
ML	Toyoura sand	$S_r=46\%$	100	1.463	72.58	18.12

536 It is obvious that PSAR greatly amplifies the permanent axial strain regardless of water content.  
537 To quantitatively describe the amplified axial strain caused by PSAR, ratio of axial strain,  
538  $(R_s)_{ave}$ , is also plotted in Fig. 20.  $(R_s)_{ave}$  is determined through dividing permanent axial strain  
539 with PSAR to that without PSAR. Consequently, all ratios are stable around 1.90 after 180  
540 loading cycles. According to previous research [Ishikawa et al., 2019b, Lin et al., 2019a],  $(R_s)_{ave}$   
541 could be roughly approximated by Eq. (28). In this case, the constant  $\beta_{PSAR}$  in Eq. (28) is deter-  
542 mined as 2.57 according to the test results that  $(R_s)_{ave}$  equals to 1.9,  $(\sigma_a)_{max}$  and  $(\tau_{a\theta})_{max}$  are 72.58  
543 kPa and 18.12 kPa respectively.

$$544 \quad (R_s)_{ave} = \exp \left( \beta_{PSAR} \frac{(\tau_{a\theta})_{max}}{(\sigma_a)_{max}} \right) \quad (28)$$

545 where  $(\sigma_a)_{max}$  is maximum axial stress;  $(\tau_{a\theta})_{max}$  is maximum shear stress;  $\beta_{PSAR}$  is material con-  
546 stant.



547

548

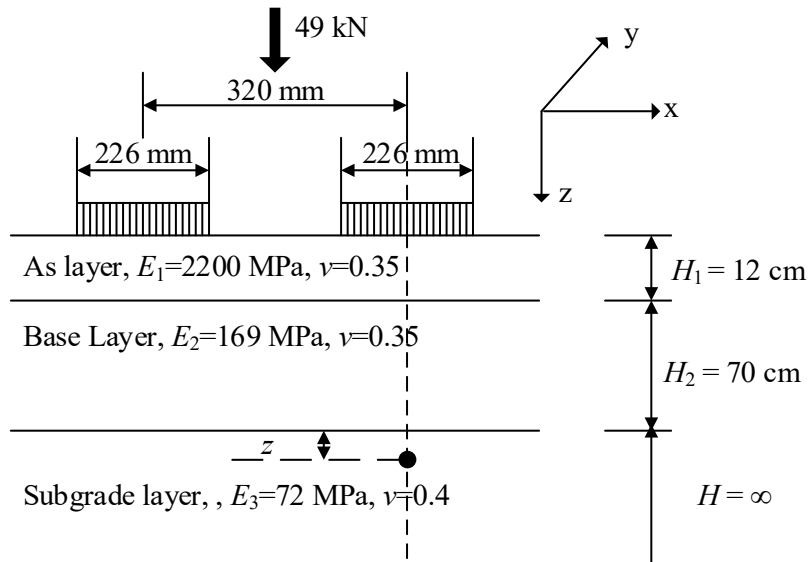
Fig. 20. Permanent axial strain of Toyoura sand.

549 As  $(R_s)_{ave}$  represents the amplification of permanent axial strain caused by PSAR, the reciprocal  
550 of  $(R_s)_{ave}$  represents the decreasing rate of failure loading number. As a result, Eq. (26) is mod-  
551 ified by adding the reciprocal of  $(R_s)_{ave}$  to capture the effect of PSAR on pavement life against  
552 rutting as shown in Eq. (29). It is noted that  $(\sigma_a)_{max}$  and  $(\tau_{a\theta})_{max}$  are stress states in laboratory  
553 test through multi-ring shear apparatus, and they are equal to vertical stress,  $(\sigma_z)_{max}$ , and shear  
554 stress,  $(\tau_{yz})_{max}$ , used in GAMES software.

$$555 \quad N_{fS} = \beta_m \cdot \beta_{s1} \cdot \{1.365 \times 10^{-9} \cdot \varepsilon_a^{-4.477 \cdot \beta_{s2}}\} / \exp\left(\beta_{PSAR} \frac{(\tau_{yz})_{max}}{(\sigma_z)_{max}}\right) \quad (29)$$

556 To apply Eq. (29) into pavement life prediction, it is necessary to determining the suitable po-  
557 sition in subgrade layer to estimate the  $(\sigma_z)_{max}$  and  $(\tau_{yz})_{max}$  through GAMES. To investigate how  
558  $(\sigma_z)_{max}$  and  $(\tau_{yz})_{max}$  change with depth, Section A and layer moduli in Aug are chosen to build a  
559 model as shown in Fig. 21. As a consequence, Fig. 22 illustrates the  $\sigma_z$  and  $\tau_{yz}$  in different depth,  
560  $z$ , and corresponding  $(R_s)_{ave}$ . It is obvious that  $\sigma_z$  and  $\tau_{yz}$  show same tendency regardless of  $h$ .  $\sigma_z$   
561 reaches the largest value just below the wheel loading ( $y=0$ ) and decreases with  $y$ . On the other

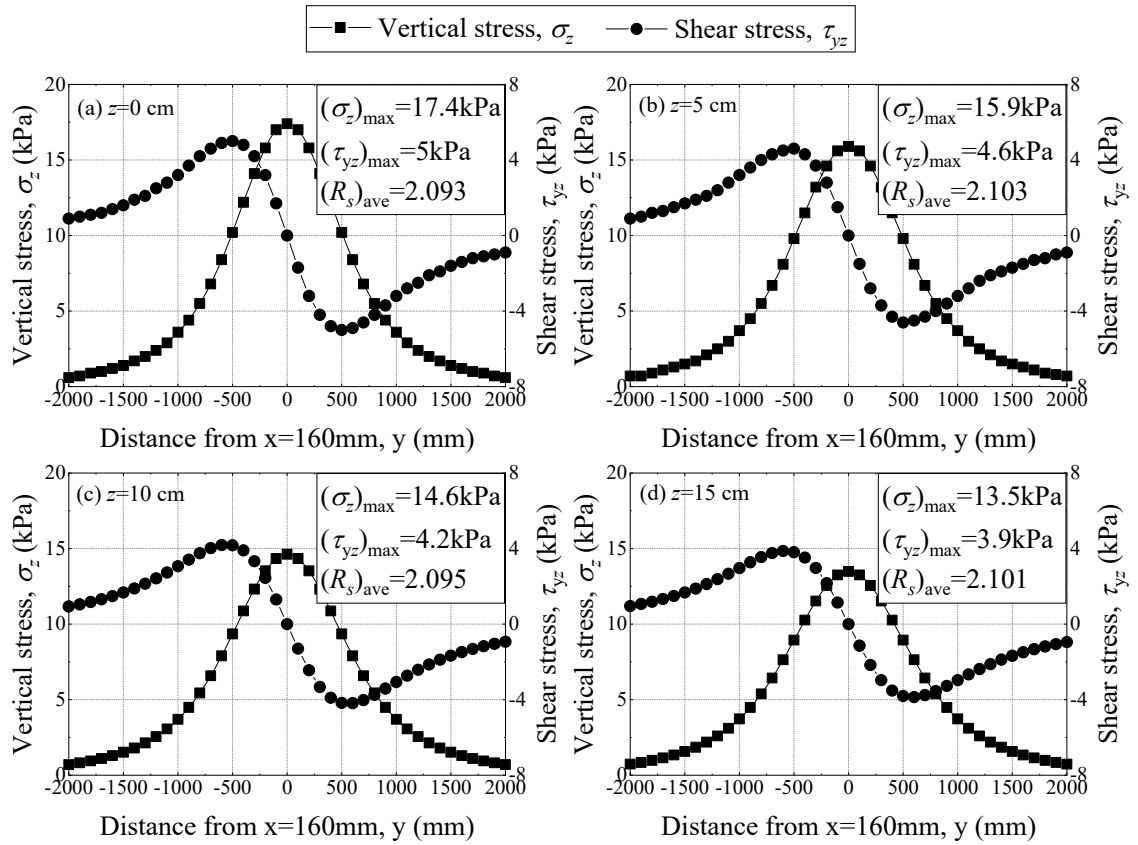
562 hands,  $\tau_{yz}$  is zero just below the wheel loading and increases to the largest value at  $y=600\text{mm}$   
 563 then decreases. When the  $z$  increases, both  $(\sigma_z)_{max}$  and  $(\tau_{yz})_{max}$  decreases.  $(R_s)_{ave}$  in all conditions  
 564 are around 2.1. Consequently, it is suggested to set the  $h$  as 10cm, same depth in convergent  
 565 analysis of  $E_3$  as shown in Fig. 12.



566

567

Fig. 21 Stress states calculation point in subgrade layer.



568

569

Fig. 22  $\sigma_z$  and  $\tau_{yz}$  in different depth and corresponding  $(R_s)_{ave}$ .

570

Allowable loading number against rutting failure calculated through Eq. (29) in all eight sec-

571

tions are shown in Fig. 23. It is obvious that PSAR greatly decreases calculated pavement life

572

and  $N_{fs}$  with considering PSAR is most close to actual measured failure loading number. It is

573

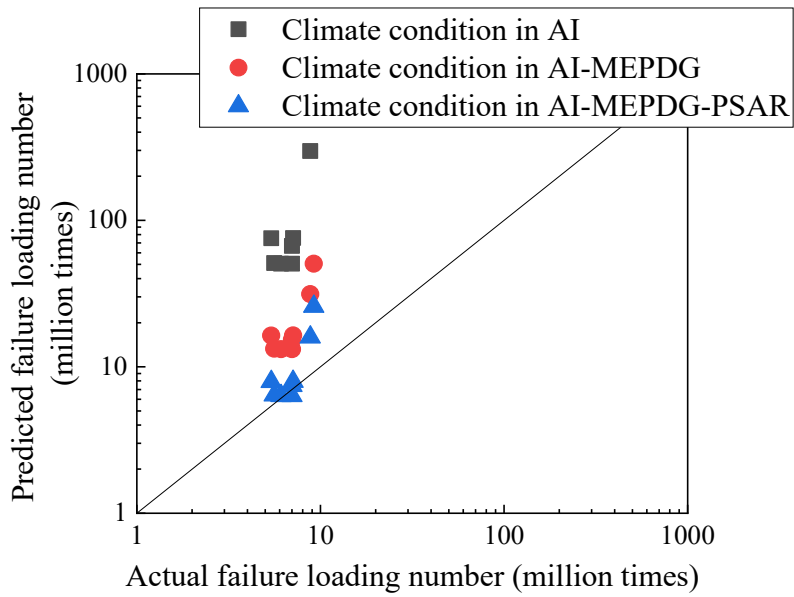
concluded the finally modified rutting model, AI-MEPDG-PSAR model, is useful and reliable

574

to predict the allowable loading number against rutting of flexible pavements especially for

575

roads located in cold regions like Hokkaido.



576

577

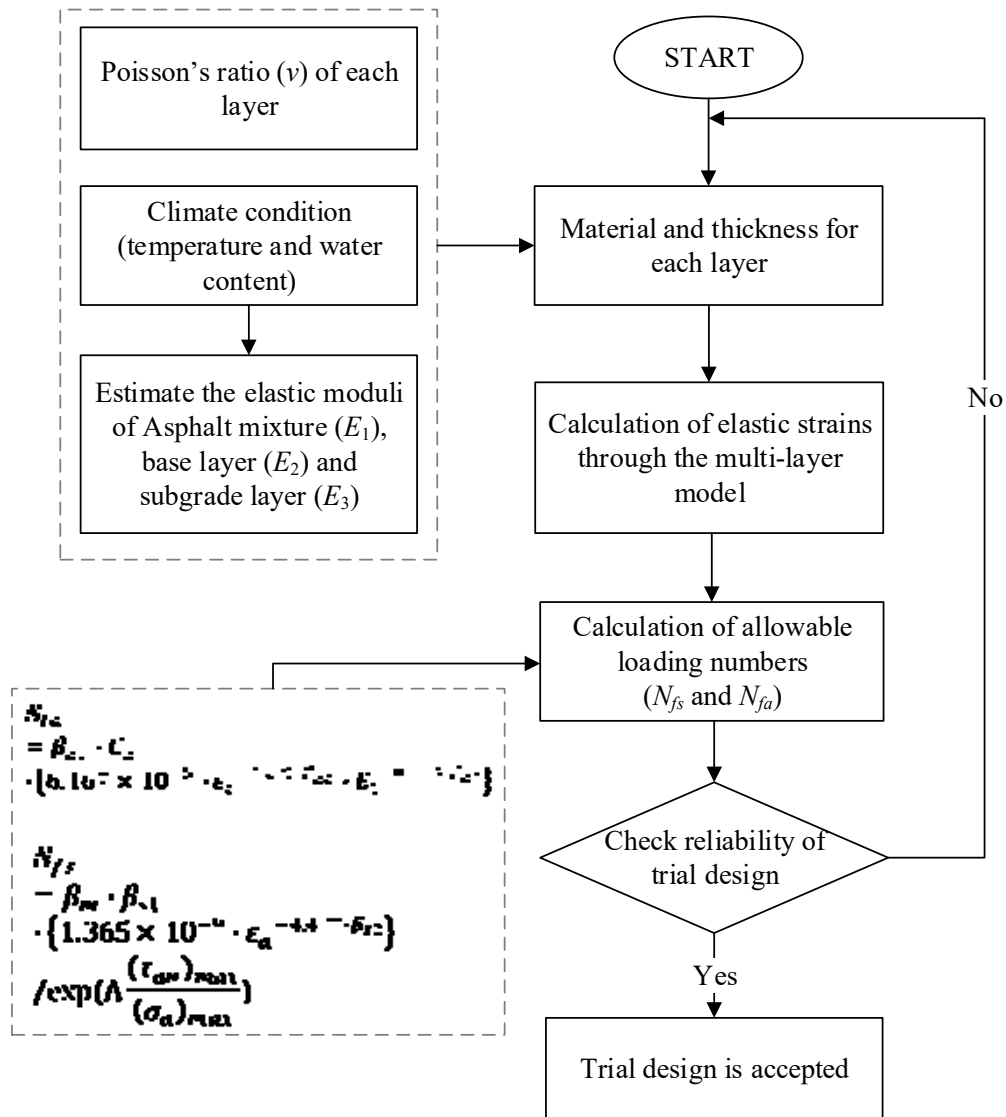
Fig. 23 Predicted  $N_{fs}$  considering PSAR.

578 Finally, the Fig. 24 illustrates the sequence in modified Japanese flexible pavement design

579 guide. It should be noted that the modification achieved in this study specially focused on the

580 base/subgrade layer mechanical properties and the rutting failure criterion as shown in the

581 comparison between Fig. 24 and Fig. 2.



582

583

Fig. 24 Sequence in modified Japanese flexible pavement design guide.

## 584 5. Conclusions

585 The following findings can be mainly obtained:

- 586 ● To modify current Japanese design guide by replacing constant subgrade layer moduli with
- 587 a variant relating to water content fluctuation and freeze-thaw history, newly proposed
- 588 modified Ng model, long-term measured in-situ base and subgrade layer water content,
- 589 and laboratory obtained SWCC are used. Calculated pavement life against rutting and fa-
- 590 tigue cracking proves that both water content fluctuation and freeze-thaw action degrade

591 stiffness of base and subgrade layer and finally decrease the pavement life of asphalt pave-  
592 ments in cold regions.

593 ● Convergence calculation are essential since the rigidity changes with pavement structures  
594 even if the influence of environmental conditions is taken into consideration. Environmen-  
595 tal condition dependence has a greater effect on pavement life in pavement structures such  
596 as high-standard roads, especially in the case of Japanese pavement where pavement life  
597 against rutting is more of a problem than fatigue cracking.

598 ● Principal stress axis rotation greatly amplifies the permanent strain compared with triaxial  
599 repeated loading test usually without such stress states. Ratio of axial strain,  $(R_s)_{ave}$ , is used  
600 to quantitatively describe the amplified axial strain caused by principal stress axis rota-  
601 tion and added into rutting failure criterion to help increasing prediction accuracy and ap-  
602 plicability.

603 These findings indicate that a detailed understanding of the mechanical behavior of the base  
604 and subgrade layer with complex water content fluctuation, freeze-thaw history, and stress  
605 states is essential to develop a mathematical model for the mechanical response of the base and  
606 subgrade layer in cold regions, and incorporate it into the theoretical design method for pave-  
607 ment structures. Besides, a modification on the structure of failure prediction model by consid-  
608 ering principal stress axis rotation is also important to improve the prediction accuracy and  
609 applicability of mechanical-empirical design method for pavement in cold regions. Conver-  
610 gence analysis is recommended for users of proposed modified design method according to its  
611 effect on resilient modulus since the incorporation of all the improvements mentioned in this  
612 study into a program for pavement design and lifetime prediction could overcome the



613 cumbersome calculations caused during the convergence analysis. Further and more compre-  
614 hensive studies including more test on unbound granular materials with various water contents,  
615 local calibration with more tests pavements are recommended to examine the validity, limita-  
616 tion of application, and so forth as these findings are obtained through limited experimental  
617 conditions and only examined with some local test pavement projects.

## 618 **Acknowledgements**

619 This research was supported in part by Grant-in-Aid for Scientific Research (B) (20360206),  
620 (C) (15K06214), and (A) (16H02360) from Japan Society for the Promotion of Science (JSPS)  
621 KA-KENHI. Support from China Scholarship Council is also highly acknowledged.

## 622 **References**

- 623 [1] AASHTO 2008. Mechanistic-Empirical Pavement Design Guide: A Manual of Practice,  
624 Washington.
- 625 [2] Aldrich HP. Frost penetration below highway and air-field pavement. Highw Res Board  
626 Bull 1956;135:124-49.
- 627 [3] Asphalt Institute 1982. Research and Development of Asphalt Institute's Thickness De-  
628 sign Manual, 9th ed. Asphalt Institute, College Park Md.
- 629 [4] ASTM, 2011, Standard Practice for Classification of Soils for Engineering Purposes  
630 (Unified Soil Classification System) (D2487-11)
- 631 [5] Berg RL, Bigl SR, Stark JA, Durell GD. Resilient modulus testing of materials from  
632 Mn/Road: phase 1. 1996. <https://doi.org/10.21949/1404573>

- 633 [6] Brown SF. Soil mechanics in pavement engineering. *Géotechnique* 1996;46(3):383-426.  
634 <https://doi.org/10.1680/geot.1996.46.3.383>
- 635 [7] Cary CE, Zapata CE. Resilient modulus for unsaturated unbound materials. *Road Mater*  
636 *Pavement Des* 2011;12(3):615–38. <https://doi.org/10.1080/14680629.2011.9695263>
- 637 [8] Clayton CRI. Stiffness at small strain: research and practice. *Geotech* 2011;61:5-37.  
638 <https://doi.org/10.1680/geot.2011.61.1.5>
- 639 [9] Cole DM, Irwin LH, Johnson TC. Effect of freezing and thawing on resilient modulus  
640 of a granular soil exhibiting nonlinear behavior. *Transp Res Rec J Transp Res Board*  
641 1981;809:19-26.
- 642 [10] Fredlund DG, Xing A. Equations for the soil-water characteristic curve. *Can Geotech J*  
643 1994;31(4):521-532. <https://doi.org/10.1139/t94-061>
- 644 [11] Fredlund MD, Wilson GW, Fredlund DG. Use of the grain-size distribution for estima-  
645 tion of the soil-water characteristic curve. *Can Geotech J* 2002;39(5):1103-1117.  
646 <https://doi.org/10.1139/t02-049>
- 647 [12] Gräbe PJ, Clayton CR. Effects of principal stress rotation on permanent deformation in  
648 rail track foundations. *J Geotech Geoenviron Eng* 2009;135(4):555-565.  
649 [https://doi.org/10.1061/\(ASCE\)1090-0241\(2009\)135:4\(555\)](https://doi.org/10.1061/(ASCE)1090-0241(2009)135:4(555))
- 650 [13] Han Z, Vanapalli SK. State-of-the-art: Prediction of resilient modulus of unsaturated  
651 subgrade soils. *Int J Geomech* 2016;16(4):04015104.  
652 [https://doi.org/10.1061/\(ASCE\)GM.1943-5622.0000631](https://doi.org/10.1061/(ASCE)GM.1943-5622.0000631)
- 653 [14] Huang YH, 2004. *Pavement Analysis and Design*, 2nd ed. Pearson Education, Inc.
- 654 [15] Inam A, Ishikawa T, Miura S. Effect of principal stress axis rotation on cyclic plastic

- 655 deformation characteristics of unsaturated base course material. *Soils Found*  
656 2012;52(3):465-480. <https://doi.org/10.1016/j.sandf.2012.05.006>
- 657 [16] Ishikawa T, Sekine E, Miura S. Cyclic deformation of granular material subjected to  
658 moving-wheel loads. *Can Geotech J* 2011;48(5):691-703. [https://doi.org/10.1139/t10-](https://doi.org/10.1139/t10-099)  
659 099
- 660 [17] Ishikawa T, Lin T, Kawabata S, Kameyama S, Tokoro T. Effect evaluation of freeze-  
661 thaw on resilient modulus of unsaturated granular base course material in pavement.  
662 *Transp Geotech* 2019a;21:100284. <https://doi.org/10.1016/j.trgeo.2019.100284>
- 663 [18] Ishikawa T, Lin T, Yang J, Tokoro T, Tutumluer E. Application of the UIUC model for  
664 predicting ballast settlement to unsaturated ballasts under moving wheel loads. *Transp*  
665 *Geotech* 2019b;18:149-162. <https://doi.org/10.1016/j.trgeo.2018.12.003>
- 666 [19] Japan Meteorological Agency, Automated Meteorological Data Acquisition System.  
667 <https://www.jma.go.jp/jp/amedas/>
- 668 [20] Japan Society of Civil Engineers, 2015. Characteristics and Evaluation of Subgrade and  
669 Base Course Materials, Japan Society of Civil Engineers, Tokyo. [in Japanese]
- 670 [21] Japan Road Association, 2006. Pavement design manual, Japan Road Association, To-  
671 kyo. [in Japanese]
- 672 [22] Johnson TC, Cole DM, Chamberlain EJ. Influence of freezing and thawing on the resili-  
673 ent properties of a silt soil beneath an asphalt concrete pavement. U.S. Cold Regions  
674 Research and Engineering Laboratory, CRREL Report 78-23. 1978. [http://hdl.han-](http://hdl.handle.net/11681/9380)  
675 [dle.net/11681/9380](http://hdl.handle.net/11681/9380)
- 676 [23] Liang RY, Rabab'ah S, Khasawneh M. Predicting moisture-dependent resilient modulus

- 677 of cohesive soils using soil suction concept. *J Transp Eng* 2008;134(1):34-40.  
678 [https://doi.org/10.1061/\(ASCE\)0733-947X\(2008\)134:1\(34\)](https://doi.org/10.1061/(ASCE)0733-947X(2008)134:1(34))
- 679 [24] Lin T, Ishikawa T, Yang J, Tokoro T. Evaluation of climate effect on resilient modulus  
680 of granular subgrade material, *Cold Reg Sci Technol* 2020. (under review)
- 681 [25] Lin T, Ishikawa T, Luo B. Applicability of modified University of Illinois at Urbana–  
682 Champaign model for unbound aggregate material with different water content, *Transp  
683 Res Rec* 2019a;2673(3):439-449. <https://doi.org/10.1177/0361198119827530>
- 684 [26] Lin T, Ishikawa T, Tokoro T. Testing method for resilient properties of unsaturated un-  
685 bound granular materials subjected to freeze-thaw action. *Japanese Geotech Soc Spec  
686 Publ* 2019b;7(2):576-581. <https://doi.org/10.3208/jgssp.v07.089>
- 687 [27] Maina JW, Matsui K. Developing software for elastic analysis of pavement structure re-  
688 sponses to vertical and horizontal surface loadings. *Transp Res Rec J Transp Res Board*  
689 2004;1896(1):107-118. <https://doi.org/10.3141/1896-11>
- 690 [28] Maruyama K, Tako J, Kasahara A. Long-term performance of asphalt pavements at bibi  
691 new test road. *J JSCE E* 2006;62(3):519-530. [in Japanese]  
692 <https://doi.org/10.2208/jsceje.62.519>
- 693 [29] Maruyama K, Tako J, Kasahara A. Fatigue failure life prediction method of asphalt  
694 pavement. *J JSCE E* 2008;64(3):416-426. [in Japanese]  
695 <https://doi.org/10.2208/jsceje.64.416>
- 696 [30] Miura K, Miura S, Toki S. Deformation behavior of anisotropic dense sand under prin-  
697 cipal stress axis rotation. *J Soils Found* 1986;26(1):36-52.  
698 <https://doi.org/10.3208/sandf1972.26.36>

- 699 [31] Mori T, Kamiya K, Chiba T, Uzuoka R, Kazama M. The functional model of the soil-  
700 water characteristic curve used the logistic function during cyclic shearing. 44th Japan  
701 national conference on geotechnical engineering, Proc dom conf. 2009. p.1519-20. in  
702 Japanese.
- 703 [32] NCHRP 2004. Guide for mechanistic-empirical design of new and rehabilitated pave-  
704 ment structures.
- 705 [33] Ng CWW, Zhou C, Yuan Q, Xu J. Resilient modulus of unsaturated subgrade soil: ex-  
706 perimental and theoretical investigations. *Can Geotech J* 2013;50(2):223-232.  
707 <https://doi.org/10.1139/cgj-2012-0052>
- 708 [34] Seed HB, CHAN CK, Monismith CL. Effects of repeated loading on the strength and  
709 deformation of compacted clay. *Highw Res Board Proc* 1955;34:541-558.
- 710 [35] Simonsen E, Janoo VC, Isacsson U. Resilient properties of unbound road materials dur-  
711 ing seasonal frost conditions. *J Cold Reg Eng* 2002;16(1):28–50.  
712 [https://doi.org/10.1061/\(ASCE\)0887-381X\(2002\)16:1\(28\)](https://doi.org/10.1061/(ASCE)0887-381X(2002)16:1(28))
- 713 [36] Simonsen E, Isacsson U. Soil behavior during freezing and thawing using variable and  
714 constant confining pressure triaxial tests. *Can Geotech J* 2001;38(4):863-875.  
715 <https://doi.org/10.1139/t01-007>